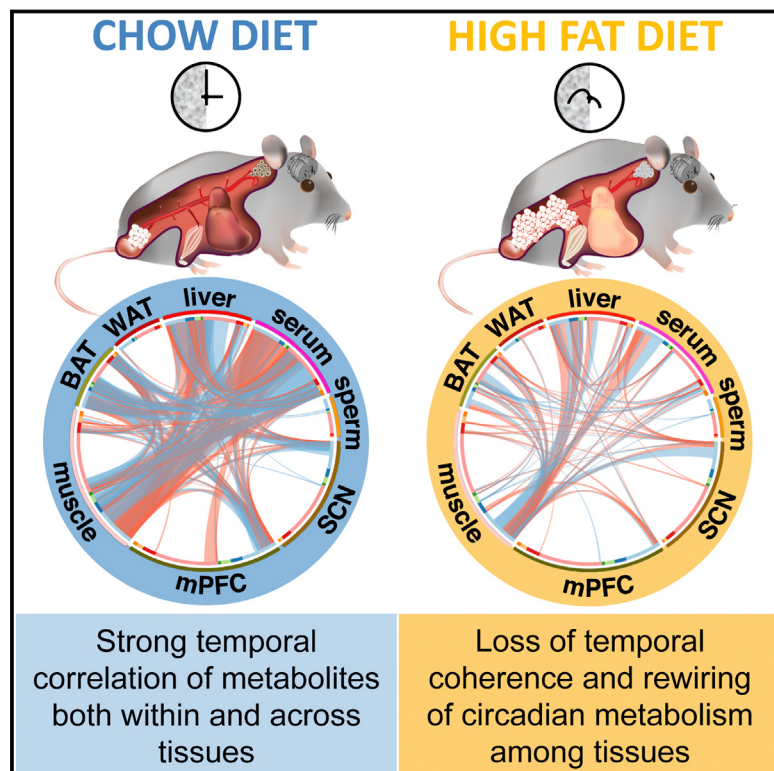


# Atlas of Circadian Metabolism Reveals System-wide Coordination and Communication between Clocks

## Graphical Abstract



## Authors

Kenneth A. Dyar, Dominik Lutter,  
Anna Artati, ..., Matthias H. Tschoöp,  
Kristin Eckel-Mahan,  
Paolo Sassone-Corsi

## Correspondence

adamski@helmholtz-muenchen.de (J.A.),  
matthias.tschoep@helmholtz-muenchen.  
de (M.H.T.),  
kristin.l.mahan@uth.tmc.edu (K.E.-M.),  
psc@uci.edu (P.S.-C.)

## In Brief

Circadian metabolite profiles of eight different tissues under standard and high-fat diet uncover highly specialized communication and coherence among tissue clocks and how this is rewired by nutrient challenge.

## Highlights

- Comprehensive atlas of 24-hr metabolism reveals temporal cohesion among tissues
- Nutrient stress disrupts circadian metabolites in a tissue-specific manner
- Communication and inter-tissue metabolite correlations are rewired by high-fat diet
- Multi-tissue metabolite correlations highlight coordinated response to metabolic challenge



# Atlas of Circadian Metabolism Reveals System-wide Coordination and Communication between Clocks

Kenneth A. Dyar,<sup>1,2,12</sup> Dominik Lutter,<sup>1,2,12</sup> Anna Artati,<sup>3</sup> Nicholas J. Ceglia,<sup>4</sup> Yu Liu,<sup>4</sup> Danny Armenta,<sup>4</sup> Martin Jastroch,<sup>1,2</sup> Sandra Schneider,<sup>5</sup> Sara de Mateo,<sup>6</sup> Marlene Cervantes,<sup>6</sup> Serena Abbondante,<sup>6</sup> Paola Tognini,<sup>6</sup> Ricardo Orozco-Solis,<sup>6</sup> Kenichiro Kinouchi,<sup>6</sup> Christina Wang,<sup>7</sup> Ronald Swerdlow,<sup>7</sup> Seba Nadeef,<sup>8</sup> Selma Masri,<sup>6</sup> Pierre Magistretti,<sup>8</sup> Valerio Orlando,<sup>8</sup> Emiliana Borrelli,<sup>6</sup> N. Henriette Uhlenhaut,<sup>1,2</sup> Pierre Baldi,<sup>4</sup> Jerzy Adamski,<sup>2,3,9,13,\*</sup> Matthias H. Tschoep,<sup>1,2,10,13,\*</sup> Kristin Eckel-Mahan,<sup>6,11,13,\*</sup> and Paolo Sassone-Corsi<sup>6,13,14,\*</sup>

<sup>1</sup>Institute for Diabetes and Obesity (IDO), Helmholtz Diabetes Center (HDC), Helmholtz Zentrum München, 85764 Neuherberg, Germany

<sup>2</sup>German Center for Diabetes Research (DZD), 85764 Neuherberg, Germany

<sup>3</sup>Institute of Experimental Genetics, Genome Analysis Center, Helmholtz Zentrum München, 85764 Neuherberg Germany

<sup>4</sup>Institute for Genomics and Bioinformatics, School of Information and Computer Sciences, University of California, Irvine, Irvine, CA 92697, USA

<sup>5</sup>Department of Genetics, University of Cambridge, Cambridge, CB2 3EH, UK

<sup>6</sup>Center for Epigenetics and Metabolism, U1233 INSERM, Department of Biological Chemistry, University of California, Irvine, Irvine, CA 92697, USA

<sup>7</sup>Harbor-UCLA Medical Center and Los Angeles Biomedical Research Institute, Torrance, CA 90509, USA

<sup>8</sup>BESE Division, KAUST Environmental Epigenetics Program, King Abdullah University Science and Technology, Thuwal, Saudi Arabia

<sup>9</sup>Chair of Experimental Genetics, Technical University of Munich, 85350 Freising-Weihenstephan, Germany

<sup>10</sup>Division of Metabolic Diseases, Technical University of Munich, 80333 Munich, Germany

<sup>11</sup>The Brown Foundation Institute of Molecular Medicine, University of Texas Health Science Center at Houston, Houston, TX 77030, USA

<sup>12</sup>These authors contributed equally

<sup>13</sup>Senior author

<sup>14</sup>Lead Contact

\*Correspondence: adamski@helmholtz-muenchen.de (J.A.), matthias.tschoep@helmholtz-muenchen.de (M.H.T.), kristin.l.mahan@uth.tmc.edu (K.E.-M.), psc@uci.edu (P.S.-C.)

<https://doi.org/10.1016/j.cell.2018.08.042>

## SUMMARY

Metabolic diseases are often characterized by circadian misalignment in different tissues, yet how altered coordination and communication among tissue clocks relate to specific pathogenic mechanisms remains largely unknown. Applying an integrated systems biology approach, we performed 24-hr metabolomics profiling of eight mouse tissues simultaneously. We present a temporal and spatial atlas of circadian metabolism in the context of systemic energy balance and under chronic nutrient stress (high-fat diet [HFD]). Comparative analysis reveals how the repertoires of tissue metabolism are linked and gated to specific temporal windows and how this highly specialized communication and coherence among tissue clocks is rewired by nutrient challenge. Overall, we illustrate how dynamic metabolic relationships can be reconstructed across time and space and how integration of circadian metabolomics data from multiple tissues can improve our understanding of health and disease.

## INTRODUCTION

Circadian clocks allow cells and tissues to compartmentalize metabolic pathways within precise temporal and spatial win-

dows (Tu and McKnight, 2006). The importance of clock function in determining health is supported by animal studies and a wealth of epidemiological evidence (Lowrey and Takahashi, 2011). Specific metabolic pathways are key regulators of circadian clocks (Rey et al., 2016; Zwighart et al., 2015), and oscillating metabolites can synchronize clocks, modulate transcription, and regulate chromatin accessibility (Aviram et al., 2016; Nakahata et al., 2009; O'Neill et al., 2008, 2011; Peek et al., 2013; Ramsey et al., 2009). Clocks across tissues are aligned under conditions of energy balance, while disruption of tissue communication is thought to increase risk of metabolic diseases (Roenneberg et al., 2012; Roenneberg and Merrow, 2016). Metabolism and circadian clocks are thus inextricably linked (Asher and Sassone-Corsi, 2015).

Metabolites reside at this important interface between circadian clocks and metabolism (Dyar and Eckel-Mahan, 2017) and are used as surrogate diagnostic and predictive biomarkers to define health or pathology (DeBerardinis and Thompson, 2012). Blood metabolite profiling is common but intrinsically limited, and few studies have combined metabolomics data from more than one tissue (Lu et al., 2017; Sugimoto et al., 2012). Providing essential temporal perspective, several groups have begun mapping metabolite dynamics over 24 hr (Aviram et al., 2016; Chen et al., 2016; Dallmann et al., 2012; Davies et al., 2014; Dyar et al., 2013; Eckel-Mahan et al., 2012; Fustin et al., 2012; Giskeødegård et al., 2015; Kim et al., 2014; Krishnaiah et al., 2017; Martinez-Lozano Sinues et al., 2014; Masri et al., 2014). Integration of 24-hr metabolomics data from multiple tissues is thus poised to push metabolite profiling



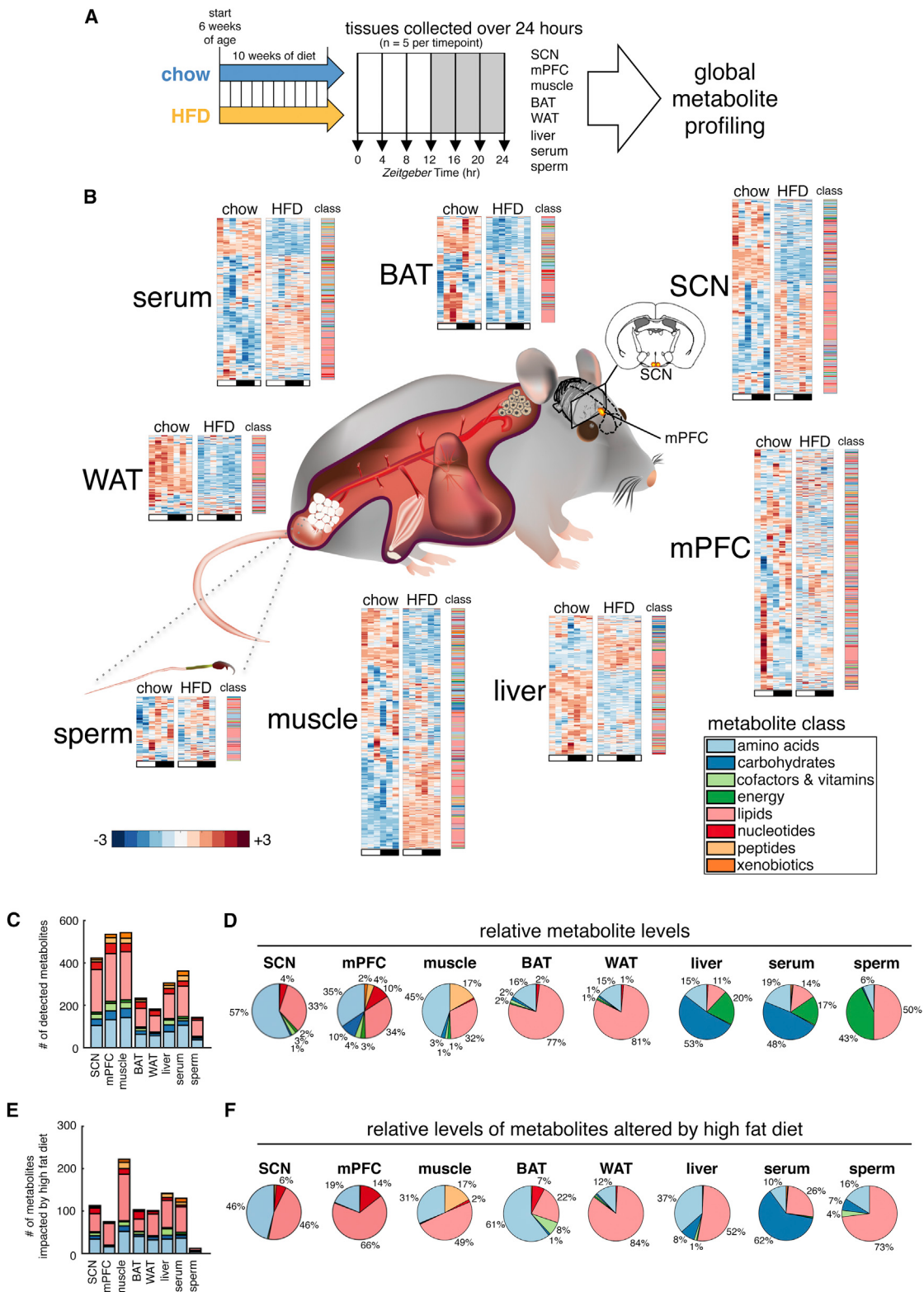


**Figure 1. Global Metabolite Profiling of Mouse Tissues over 24 hr Reveals Common and Tissue-Specific Metabolic Signatures on Chow and HFD**

(A) Experimental design. Suprachiasmatic nucleus (SCN), medial prefrontal cortex (mPFC), gastrocnemius skeletal muscle, interscapular brown adipose tissue (BAT), epididymal white adipose tissue (WAT), liver, serum, and cauda epididymal sperm collected every 4 hr across the light/dark cycle from a single cohort of mice. (legend continued on next page)

**Table 1. Percent Metabolites Impacted by HFD (Diet Effect p < 0.05, Linear Regression Model)**

tissue	%
WAT	63
liver	55
BAT	52
muscle	43
serum	41
SCN	27
mPFC	14
sperm	8

beyond simple diagnostics and biomarker detection (Brown, 2016; Goodacre, 2007) and toward actionable knowledge for preventative medicine and better predictions of how metabolite profiles can be controlled to affect a desired metabolic outcome (German et al., 2005; Gooley and Chua, 2014).

Here, we present global 24-hr metabolite profiles of eight different tissues under conditions of energy balance (standard chow) or chronic nutrient stress (high-fat diet [HFD]). We reveal how metabolic pathways are gated to specific temporal and spatial windows and how novel tissue-specific and inter-organ 24-hr dynamics emerge under HFD. Our Resource highlights temporal links between muscle insulin resistance, hepatic steatosis, atherosclerosis, and reduced energy expenditure.

## RESULTS

### Temporal and Tissue-Specific Metabolite Profiling

We performed 24-hr metabolomics profiling on eight different murine tissues: suprachiasmatic nucleus (SCN), medial prefrontal cortex (mPFC), gastrocnemius skeletal muscle, interscapular brown adipose tissue (BAT), epididymal white adipose tissue (WAT), liver, serum, and cauda epididymal sperm (Figure 1A). Tissues were collected every 4 hr across the light/dark cycle from a single cohort of C57BL/6J mice after 10 weeks of *ad libitum* access to standard chow or HFD. Mice fed HFD had rhythmic energy intake indistinguishable from chow-fed mice (Eckel-Mahan et al., 2013). Hundreds of metabolites covering a range of metabolite classes were detected in each tissue by mass spectrometry (liquid chromatography [LC/MS] and gas chromatography [GC/MS]) (Figures 1B and 1C). All data are available on CircadiOomics (<http://circadiomics.igb.uci.edu/>) (Patel et al., 2012), including interactive networks to explore the data.

Tissue-specific differences in metabolite number, temporal oscillations, and impact of HFD were apparent (Figure 1B). While

class distribution was similar across tissues (Figure 1C), relative metabolite abundance reflected tissue composition (Figure 1D): WAT and BAT revealed mostly lipids; brain and muscle showed amino acids and lipids; liver and serum showed mostly carbohydrates and comparable amounts of amino acids, lipids, and energy metabolites; sperm contained mostly lipids and energy metabolites.

The impact of HFD varied among tissues (Figures 1C and 1E). While ~540 total metabolites were detected in both mPFC and muscle, >3-fold more metabolites were altered by HFD in muscle than in mPFC (232 significantly impacted in muscle versus 75 in mPFC). Overall, WAT, liver, BAT, muscle, and serum were most impacted by HFD, with 40%–60% of detected metabolites showing significant alterations (Table 1). Brain and sperm metabolites appeared more resistant to diet-induced metabolite alterations, with SCN, mPFC, and sperm showing alterations in only 27%, 14%, and 8% of metabolites, respectively.

Subpathway enrichment analysis of significantly altered metabolites (Table S1) identified specific lipid classes altered by HFD, including long-chain fatty acids, polyunsaturated fatty acids (PUFA), diacylglycerols, phospholipids, sphingolipids, glycerolipids, and lysolipids. Metabolites involved in amino acid metabolism, particularly the urea cycle metabolites arginine and proline but also lysine, branched-chain amino acids (BCAA) leucine, isoleucine and valine, and dipeptides were also highly impacted.

Altered abundance of metabolites suggested tissue pathology (Figure 1F). For example, carbohydrates comprised 53% of liver metabolites on chow and made up only 8% altered by HFD, while lipids comprised only 11% on chow yet 52% altered by HFD (Figure 1D), suggesting hepatic steatosis. Skeletal muscles on HFD exhibited a large accumulation of lipids known to negatively impact insulin sensitivity.

### Tissue-Specific Impact of HFD on 24-hr Metabolism

Comparing circadian metabolites (i.e., oscillating with a 24-hr period) revealed major differences in how 24-hr metabolism is organized among different tissues. Serum, BAT, liver, skeletal muscle, and mPFC are all highly dynamic tissues (Figure 2), with 20%–50% of metabolites showing 24-hr oscillation regardless of diet. While lipids comprised the largest class detected in each tissue (Figure 1C), the numbers of cycling lipids varied widely among tissues on both diets (Figure 2). For example, we detected more cycling lipids in BAT, mPFC, and serum on chow compared to SCN, muscle, WAT, and liver. Furthermore, BAT, mPFC, and serum all lost lipid oscillation on HFD, while SCN surprisingly gained ~100 *de novo* oscillating lipids. We also noted a marked temporal gating of 24-hr cycling lipids to the light phase in mPFC, BAT, and serum

C57BL/6J mice. Six time points were profiled for SCN, mPFC, muscle, and sperm; a 7<sup>th</sup> replicate time point, ZT24, was additionally profiled for serum, liver, BAT, and WAT.

(B) Tissue-specific metabolite heatmaps. Rows reflect normalized (Z score) metabolite abundance across the light/dark cycle (white bar, ZT0, 4, 8, and 24; black bar, ZT12, 16, and 20). Metabolite class is indicated at the right of each heatmap.

(C) Counts and class of detected metabolites for each tissue.

(D) Tissue metabolite class composition according to relative metabolite masses (sum of standardized abundances).

(E) Counts and class of metabolites significantly impacted by diet (diet effect p < 0.05, linear regression model).

(F) HFD-altered metabolite class composition for each tissue (relative metabolite masses affected by HFD).

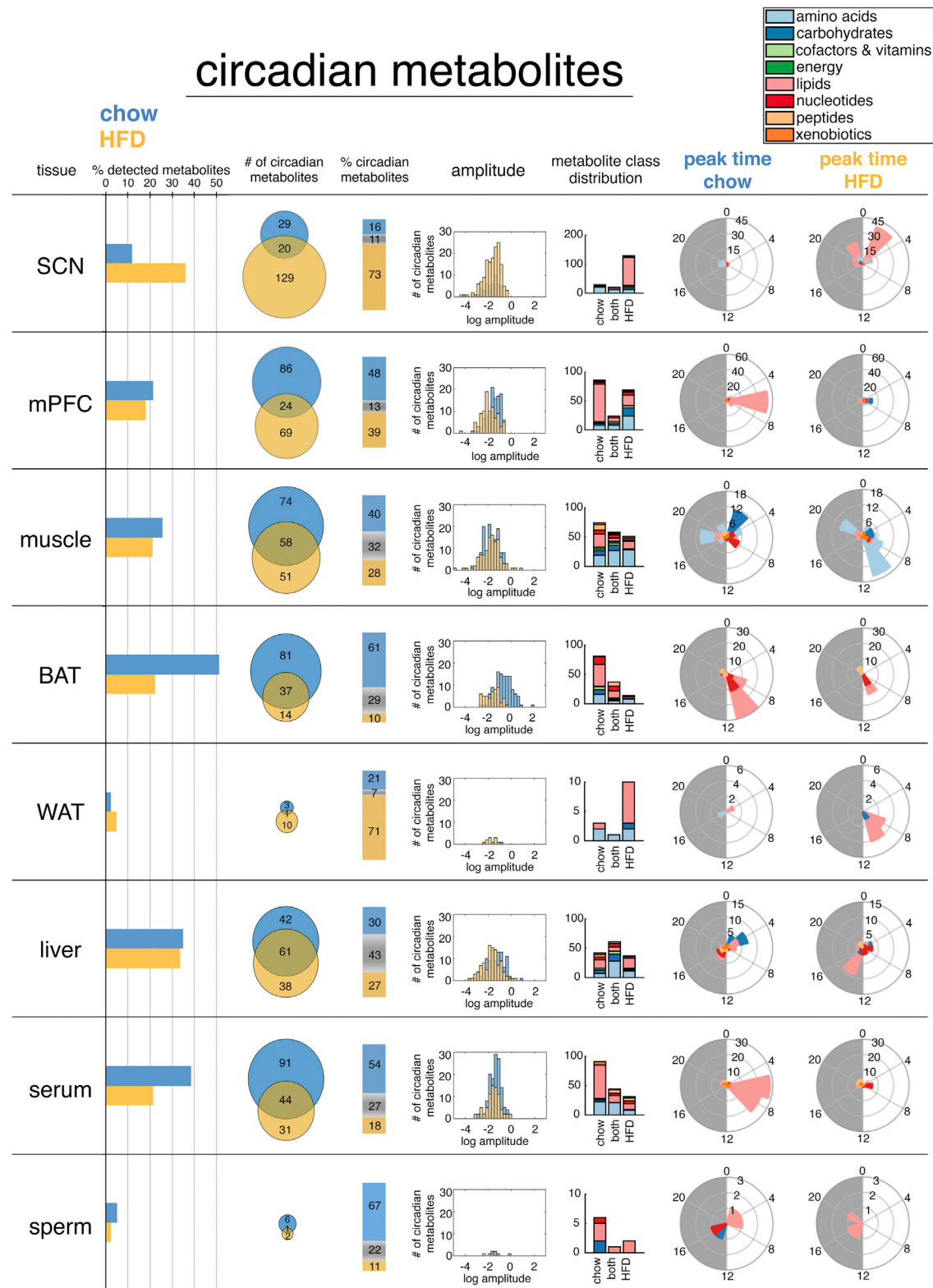


**Figure 2. Comparative Analysis of Circadian Metabolites Highlights Heterogeneity of Tissue Circadian Function**

24-hr oscillating metabolites ( $p < 0.05$ , JTK\_CYCLE) for each tissue are plotted from left to right according to (1) relative % of detected metabolites, (2) absolute numbers, (3) % distribution, (4) amplitude of oscillation, (5) class distribution, and (6) and (7) phase distribution.

on chow, with peaks slightly different in each tissue. Lipids peaked around *Zeitgeber* time (ZT) 6 in mPFC, ZT6–ZT8 in serum, and ZT8–ZT10 in BAT.

Skeletal muscle showed a more diverse and temporally compartmentalized distribution of 24-hr cycling metabolite peaks on chow. Carbohydrates peaked around ZT2, whereas nucleotides peaked around ZT8, and amino acids around ZT18. Amino acid peaks were drastically altered on HFD, shifting to around ZT8–ZT10 with a secondary peak at ZT20, highlighting a massive reorganization of muscle amino acid metabolism on HFD. Disease-associated metabolite enrichment (Xia and Wishart, 2016) of these revealed an association with “degradation of skeletal muscle,” highlighting a potential pathologic underpinning. Indeed, short-term HFD in mice accelerates skeletal muscle atrophy of the soleus upon denervation (Roseno et al., 2015), while 16 weeks of chronic HFD in rats causes gastrocnemius atrophy and upregulation of ubiquitin ligase *Murf1* (Sishi et al., 2011).

Cauda epididymal sperm (Figures S1A and S1B) displayed relatively few oscillating metabolites (Figure 2). However, glycolytic intermediates 2- and 3-phosphoglycerate oscillated only on chow (Figure S1C), while more than 40% of all lysolipids were significantly reduced during the dark phase on HFD (Figure S1D).

Circadian metabolite subpathway enrichment revealed common and tissue-specific metabolite classes (Table S2). Independent of diet, serum and muscle maintained robust 24-hr oscillation of BCAA metabolites, while on HFD, both serum and muscle gained additional circadian enrichment of metabolites involved in glycine, serine, and threonine metabolism. Muscle further gained 24-hr oscillation of metabolites related to alanine and aspartate metabolism on HFD, while BAT gained oscillation of guanine-containing purine nucleotides.

### Metabolite Correlations Reveal Tissue-Specific Temporal Gating of Metabolic Pathways

Coherent temporal gating of metabolic pathways is essential for maintenance of tissue homeostasis (Noguchi et al., 2013). We hypothesized that metabolites sharing positive temporal correlation may have common origins or functions and belong to related metabolic networks, whereas metabolites with negative correlation may reflect temporal gating of incompatible pathways. Furthermore, temporal correlation of metabolites can serve as a general index for synchronization of individual cells within a tissue, since dynamic pathways should be highly correlated among synchronized cells. We found extensive positive and negative temporal correlations among metabolites in all tissues (Figures 3A and 3B), and interestingly, many tissues lost metabolite correlations on HFD. Serum and BAT lost 98% and 74%, respectively, whereas liver and muscle lost only 34% and 39%, respectively. This suggests maintenance and/or reorganization of metabolic pathways in liver and muscle. On the other hand, the severe loss of intra-tissue metabolite correlations in serum has major implications for how misalignment among tissues may be exacerbated by nutritional challenge.

We next visualized significant positive and negative temporal correlations according to metabolite class (Figure 3C). Serum lipids showed the greatest degree of temporal correlation with other metabolites, especially amino acids. Importantly, these were severely reduced on HFD, with serum amino acids and

peptides gaining correlations. Major positive correlations among BAT nucleotides, lipids, and amino acids were lost on HFD. While muscle and liver similarly lost temporal correlation among metabolite classes, they also maintained substantial metabolite correlations on HFD, particularly among amino acids and carbohydrates.

Subpathway enrichment analysis of significantly correlated metabolites revealed maintenance of carbohydrate correlations on HFD, with muscle glycolytic intermediates and liver sugar metabolites retaining temporal correlation (Table S3), in agreement with enrichment analysis (Table S2). However, serum lost correlation among essential fatty acids on HFD, in addition to several medium chain fatty acids, and lysolipids, while muscle lost correlation among acylcarnitines, as well as tricarboxylic acid (TCA, or Krebs) cycle metabolites. Furthermore, both serum and muscle gained correlations among BCAA and other amino acids on HFD, suggesting a coordinated response.

Using temporal associations, one can reconstruct metabolic pathways over 24 hr. For example, muscle glycolytic intermediates and acylcarnitines respectively reflect cytosolic or mitochondrial ATP production. Both metabolite classes showed dynamic oscillation over 24 hr (Figure 3D). On chow, peaks were confined to distinct temporal windows, reflecting delineation of diurnal fuel preference. Glycolytic intermediates declined across the light phase, whereas acylcarnitines increased toward the end. Acylcarnitines were lowest in the middle of the dark phase when glycolytic intermediates were increased. However, on HFD oscillation of glycolytic intermediates was blunted during the dark phase, while acylcarnitines remained at peak levels. These coordinated metabolite alterations imply impaired metabolic flexibility and may contribute to insulin resistance.

### Inter-tissue Clock Communication: Metabolite Coherence or Dissonance

Visualization of inter-tissue metabolite temporal correlations revealed metabolic coupling between tissues (Figure 4A). Importantly, serum emerged as a main source of metabolite correlations on chow, underscoring the role of circulating factors in temporal communication, as serum metabolites both direct and reflect tissue-specific metabolism. HFD was associated with a severe loss of temporal coherence (Figure 4B), specifically between serum and muscle, liver, and BAT (Figures 4C). Comparative inspection of cross-tissue correlations between serum, liver, muscle, and BAT further emphasized HFD-induced loss and reorganization of metabolite correlations (Figure 5). Normally abundant liver-serum and muscle-serum metabolite correlations were reduced ~60% on HFD (Figure S2A), while BAT-serum correlations were reduced 74%. Lipids and amino acids were the main metabolite classes correlated between serum and other tissues on chow, comprising ~60%–70% of all significant inter-tissue metabolite correlations. Interestingly, BAT and serum nucleotides showed a relatively high degree of temporal correlation. Importantly, most cross-tissue metabolite correlations were lost on HFD (Figure S2B), with inter-tissue lipids losing ~80% in all tissues and amino acids losing 35%–66%, depending on the tissue (Figure S2C). A majority of HFD inter-tissue metabolite correlations were not shared on chow. These *de novo* correlations were especially prevalent among

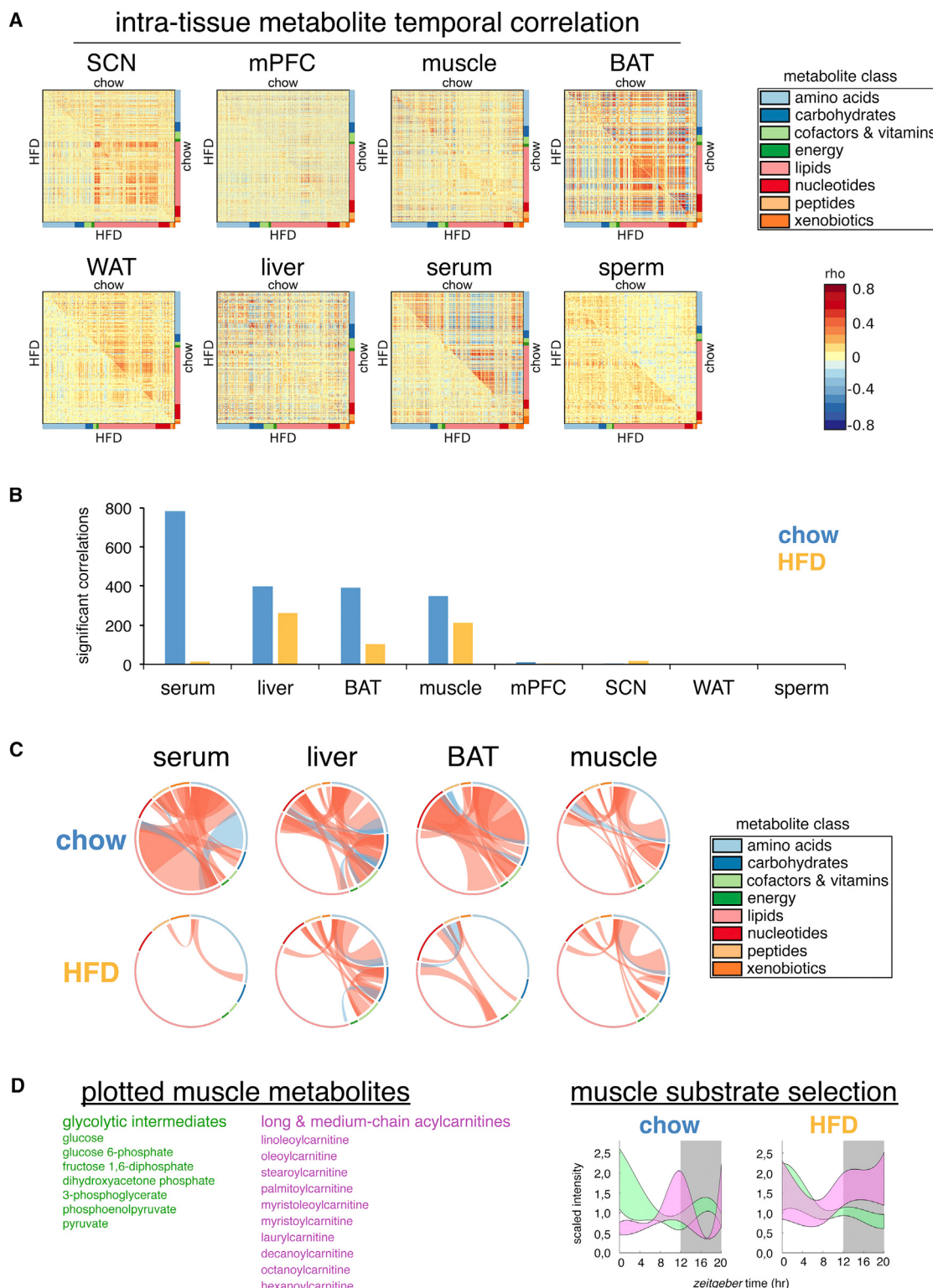


**Figure 3. Tissue-Specific Metabolite Correlations Illustrate How Temporal Coherence and Normal Gating of Metabolic Pathways Is Maintained or Altered by HFD**

(A) Correlation heatmaps for metabolites in each tissue. Correlation coefficient rho is shown as red (positive) or blue (negative) as indicated.  
(B) Number of significant metabolite correlations according to tissue and diet.

(legend continued on next page)

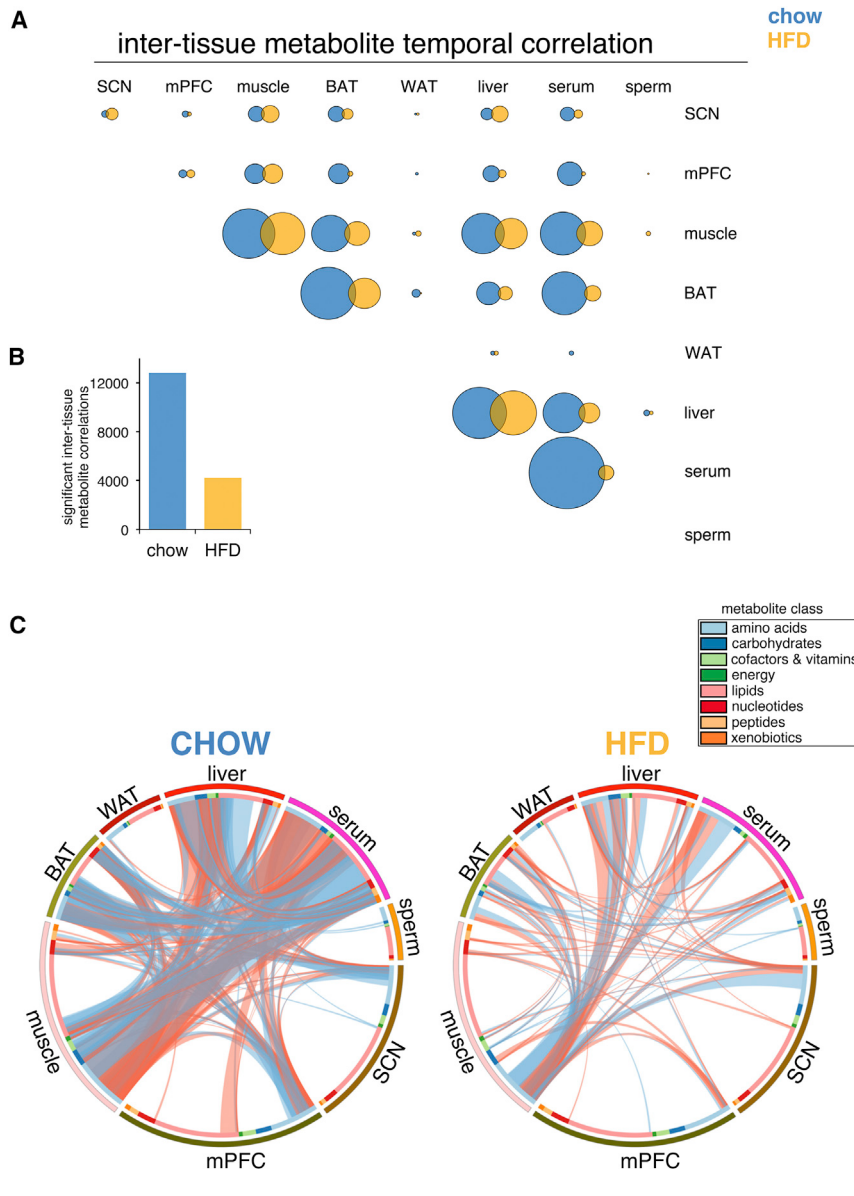


**Figure 4. Loss of Inter-tissue Metabolite Correlations on HFD**

(A) Correlated metabolites between each tissue. Circle areas sized according to number of significant metabolite correlations.

(B) Significant inter-tissue metabolite correlations.

(C) Graphical summary of all inter-tissue metabolite temporal correlations. Each ribbon indicates a significant inter-tissue metabolite correlation (positive, red; negative, blue). Ribbon thickness refers to number of significantly correlated metabolites.

were gated to distinct temporal windows on chow, oscillating anti-phase to one another (Figure 6A). However, circulating alanine remained relatively stable across the circadian cycle in chow-fed mice yet on HFD became highly oscillatory and increased during the light phase. This effect was even more pronounced in skeletal muscle on HFD, with alanine levels constitutively elevated across the light phase. There were no major HFD-induced changes in alanine levels in liver or WAT, whereas BAT showed slightly reduced levels.

Increased alanine production and release by skeletal muscle normally occurs in response to increased protein catabolism during periods of starvation (Felig, 1973). The rate of muscle protein degradation is often clinically inferred by levels of 3-methylhistidine, a unique amino acid released by myofibrillar proteolysis and excreted in the urine (Elia et al., 1981). We detected 3-methylhistidine only in serum and skeletal muscle, with both tissues showing 24-hr oscillation on chow and HFD (Figure 6B). However, peak 3-methylhistidine was significantly increased on HFD, suggesting increased muscle protein degradation. We also

muscle, serum, and liver amino acids, again highlighting coordinated metabolic responses linking these tissues.

#### Increased Muscle Protein Turnover on HFD Linked to Increased Liver Gluco- and Glyceroneogenesis

Our data revealed significant HFD-specific metabolite correlations and *de novo* oscillations linking increased muscle protein degradation to liver gluco- and glyceroneogenesis. We noted diurnal rhythms of glutamine and alanine in muscle and liver

noted increased creatinine in serum on HFD and a similar trend in muscle, indicating that muscle mass is maintained or even slightly increased despite protein breakdown and suggesting increased overall rates of muscle protein turnover on HFD.

The majority of alanine released from muscle is synthesized *de novo* by transamination of pyruvate, with nitrogen originating mostly from BCAA via glutamate (Odessey and Goldberg, 1979). Serum, muscle, and liver BCAA showed 24-hr oscillation on chow and HFD, with increased levels during the dark phase

(C) Graphical visualization of significant metabolite correlations. Each ribbon indicates a significant metabolite correlation (positive, red; negative, blue) between or within each metabolite class. Ribbon thickness refers to number of significantly correlated metabolites. Metabolites were ordered according to metabolite class as indicated in colored bar around the circumference.

(D) “Fuzzy plots” show the range (colored area) between minimum and maximum abundance for members of each metabolic pathway. Cubic-splines interpolation estimated continuous abundance.

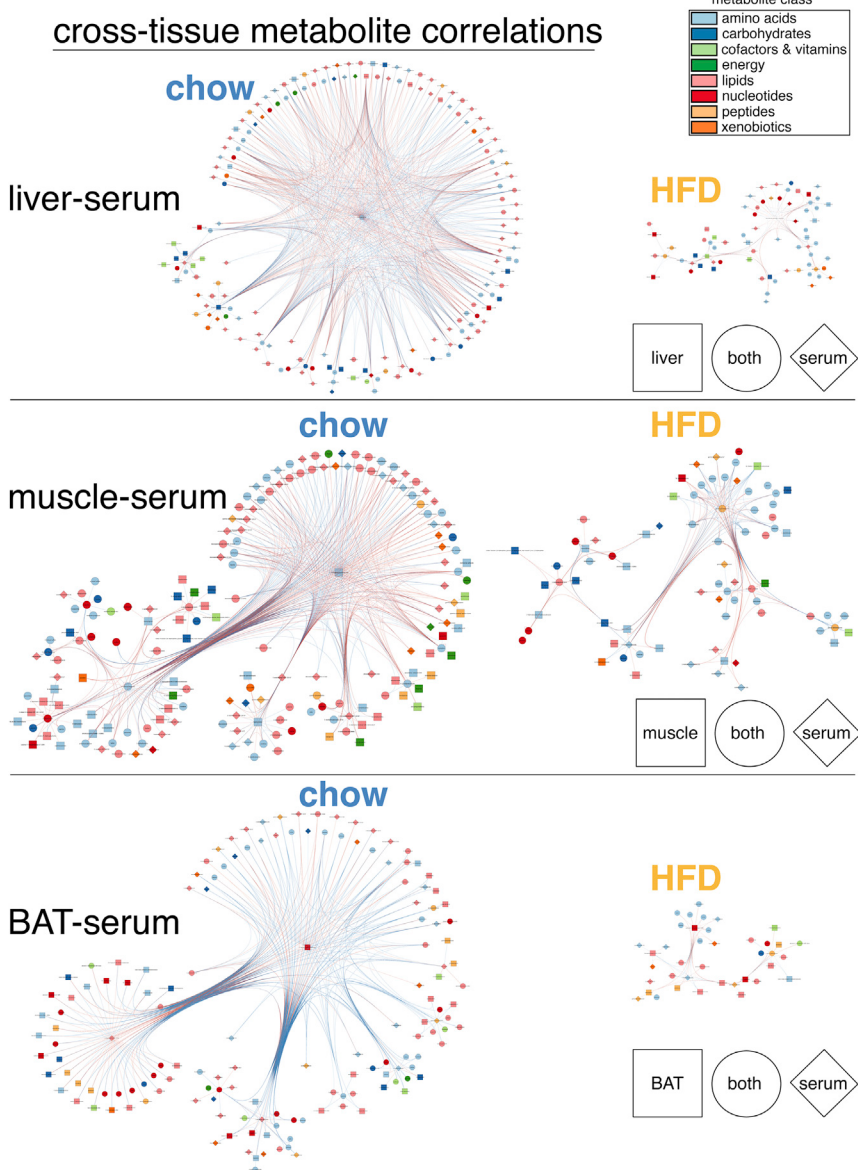


**Figure 5. Serum, Liver, Muscle and BAT Cross-Tissue Metabolite Correlations Severely Altered by HFD**

Networks of significantly correlated metabolites detected on chow or HFD. Each node refers to a single metabolite. Node shape indicates tissue or tissues showing correlation. Node color refers to metabolite class. Edges are drawn for each significant inter-tissue correlation, and edge colors refer to the sign of correlation coefficient (red, positive; blue, negative).

WAT, and BAT (Figure S3A), possibly reflecting increased rates of gluco- and glyceroneogenesis in liver (Song et al., 2001) and reduced amino acid uptake and metabolism in WAT and BAT (Serra et al., 1994). Moreover, glycerol 3-phosphate, a major precursor for liver glyceride-glycerol and very low density lipoprotein (VLDL) synthesis (Nye et al., 2008), was increased ~50% across the day/night cycle on HFD (Figure 6C) and oscillated in phase with muscle and serum alanine, indicating increased conversion of serum alanine (and other glucogenic amino acid substrates resulting from muscle protein degradation) to liver glyceride-glycerol (Nye et al., 2008).

Muscle protein degradation and liver gluco- and glyceroneogenesis are under tight hormonal control, mainly by opposing actions of circulating glucocorticoids and insulin (Hatting et al., 2018; Schiaffino et al., 2013; Shimizu et al., 2015). The temporally linked rise and fall of muscle and serum 3-methylhistidine on chow largely reflected 24-hr oscillation of endogenous serum corticosterone (Figure 6D) and insulin (Jouffe et al., 2016). Interestingly, serum corticosterone levels were not increased and oscillated normally on HFD. This is intriguing,

considering associations between chronic HFD and insulin resistance of skeletal muscle and liver (Oakes et al., 1997) largely mirror metabolic complications associated with chronic glucocorticoid administration, including impaired insulin-dependent glucose uptake and metabolism by muscle and reduced insulin-mediated suppression of hepatic glucose production, leading to hyperglycemia (Dunford and Riddell, 2016). Our results indicate that chronic HFD may locally enhance sensitivity to the effects of endogenous glucocorticoids. Indeed, serum glucose remained constitutively elevated on HFD, while oscillation of glucose in liver and muscle in chow-fed mice was blunted and likewise elevated, but only at ZT12 (Figure 6E), corresponding to the peak of endogenous glucocorticoids.

and reduced levels during the light phase (Figure S3A). Serum and muscle from HFD mice also showed increased BCAA levels at various time points compared to chow mice, whereas BCAA levels in liver, WAT, and BAT were all significantly reduced on HFD. While most amino acids are transaminated in the liver, BCAA are transaminated mainly in skeletal muscle, resulting in formation of branched-chain keto acids (BCKA)  $\alpha$ -ketoisocaproate,  $\alpha$ -ketomethylvalerate, and  $\alpha$ -ketovalerate. All three BCKAs were drastically reduced and lost 24-hr oscillation in muscle on HFD (Figure S3B), yet serum BCKA levels were significantly increased, suggesting augmented export from muscle and/or reduced uptake from other tissues.

Another striking effect of HFD was the specific increase of glucogenic amino acids in muscle and serum, with reduction in liver,

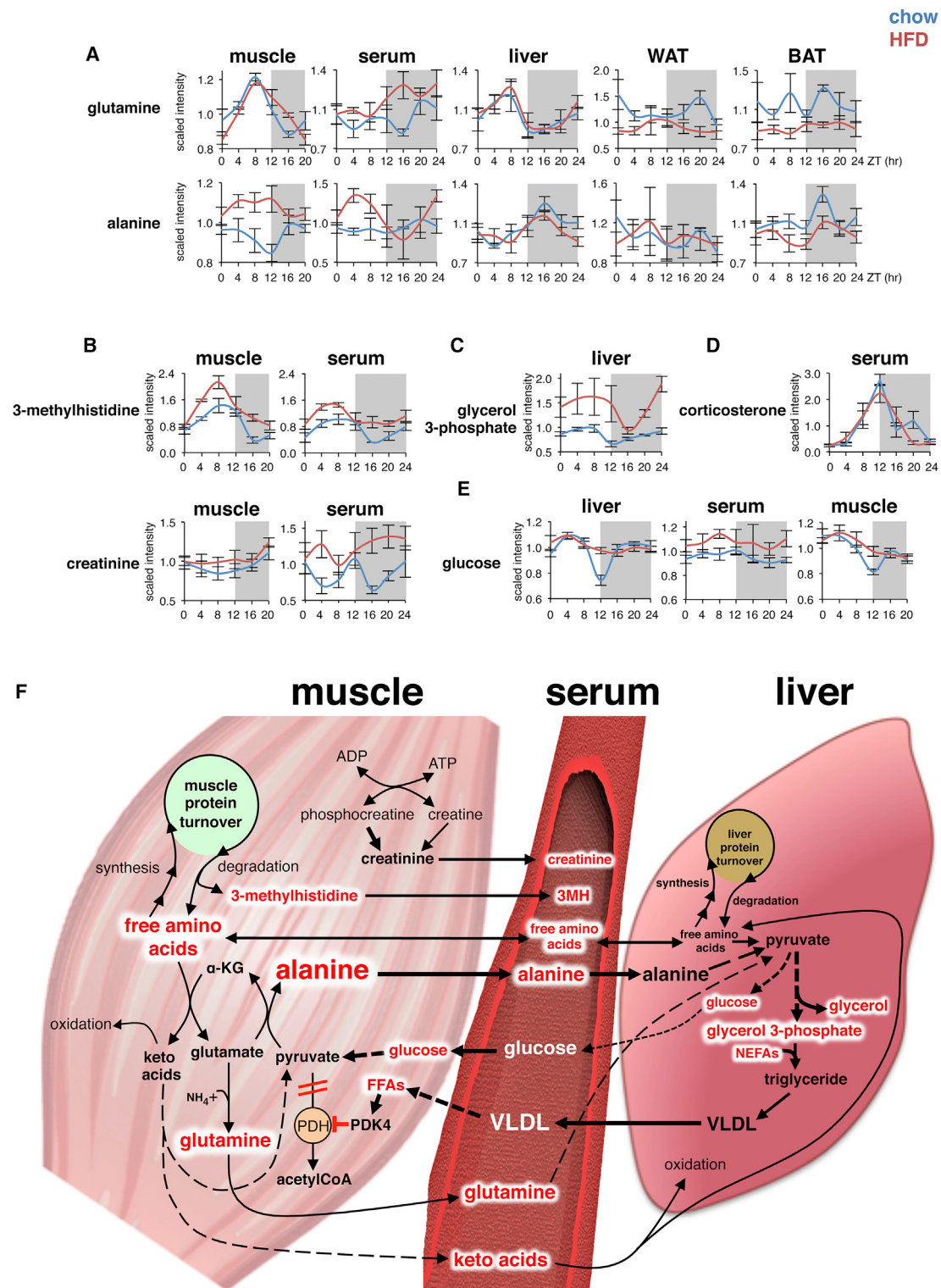


**Figure 6. Increased Circadian Oscillation of Muscle and Serum Metabolites Linked to Increased Liver Precursors for Gluco- and Glyceroneogenesis**

(A–E) Diurnal variations of selected metabolites in mouse tissues on chow or HFD (mean  $\pm$  SEM; n = 5  $\times$  group  $\times$  time point).

(F) Simplified scheme showing interrelationships between HFD-induced metabolite alterations detected muscle, serum, and liver. Red text indicates metabolites significantly increased by HFD.

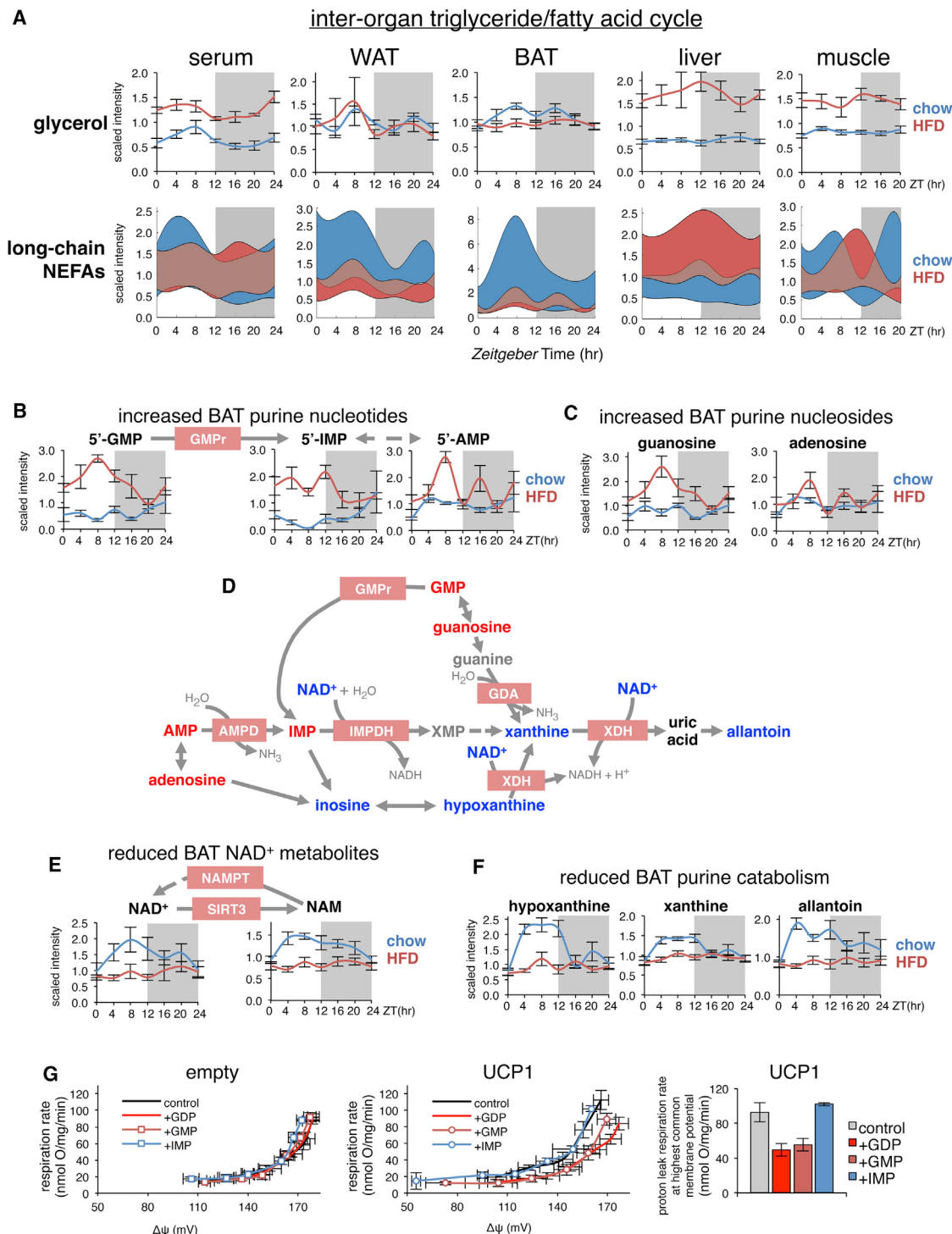


**Figure 7. Loss of Circadian Lipid Oscillation in BAT Linked to Reduced Purine Catabolism, De Novo Oscillation of Purine Nucleotides, and Impaired UCP1 Activation**

(A) Representative diurnal variations of substrates from the inter-organ triglyceride and fatty acid cycle in relevant tissues (mean  $\pm$  SEM;  $n = 5 \times$  group  $\times$  time point). “Fuzzy plots” of all detected medium- and long-chain nonesterified fatty acids (NEFAs) indicate the range (colored area) between minimum and maximum abundance for all medium- and long-chained NEFAs.

(B and C) Diurnal variations of BAT purine nucleotides and nucleosides (mean  $\pm$  SEM;  $n = 5 \times$  group  $\times$  time point). GMP reductase (GMPr) converts GMP to IMP.

(legend continued on next page)

The proposed pathogenic relationships between muscle, serum, and liver metabolites increased on HFD are summarized in **Figure 6F**. Increased cycles of muscle protein turnover lead to increased production and release of alanine and other amino acids destined for uptake mostly by the liver. The importance of serum alanine is supported by arteriovenous differences in rat and human, showing preferential hepatic uptake of alanine above all other amino acids (Pozefsky et al., 1969). Glutamine is the only amino acid released by muscle at higher rates than alanine, and it is destined mostly for kidneys and small intestine, which in turn release alanine (Snell and Duff, 1979). Excess amino acids not utilized for liver protein synthesis may be metabolized and converted to glucose and glyceride-glycerol, contributing to elevated glycemia, increased production of hepatic triacylglycerol (TAG), and secretion of VLDL. Hypertriglyceridemia and increased VLDL secretion are associated with metabolic diseases linked to poor diet, lack of exercise, and obesity, including insulin resistance and cardiovascular disease (Eckel et al., 2005). Increased muscle free fatty acids (FFAs) may activate pyruvate dehydrogenase kinase 4 (PDK4), inhibiting pyruvate dehydrogenase, further promoting alanine production (Zhang et al., 2014). Our data suggest that muscle protein turnover, and particularly muscle alanine production and release, may play a previously underappreciated pathogenic role in metabolic diseases.

#### ***De novo Oscillation of Purine Nucleotides in BAT on HFD Linked to Impaired UCP1 Activity***

Tissue-specific changes in glycerol and non-esterified fatty acids (NEFA) reflect continuous turnover and transport of lipids among tissues in a state of so-called dynamic equilibrium (Guggenheim, 1991), in which total body fat content remains constant in the midst of high rates of degradation, inter-conversion, and re-esterification of lipid stores within and across tissues over 24 hr. Interestingly, HFD blunted oscillation of circulating NEFAs, increased levels of serum glycerol, and severely reduced NEFA levels and oscillation in WAT and BAT (**Figure 7A**), suggesting an impaired diurnal turnover of lipid stores in both fat depots. In contrast, liver glycerol and NEFAs were dramatically increased on HFD, similar to skeletal muscle, highlighting known pathological deposition of biologically active lipids associated with obesity and insulin resistance. The massive reduction in circadian BAT NEFAs is of interest, since they directly stimulate thermogenic proton leak via activation of uncoupling protein 1 (UCP1) (Nicholls and Locke, 1984).

In absence of activating fatty acids, extra-mitochondrial purine nucleotides restore energy conservation in BAT mitochondria by directly binding and inhibiting UCP1 (Shabalina et al., 2004). Guanine nucleotides show higher recoupling efficiency than

adenine nucleotides due to their higher affinity for UCP1 and higher concentration in the mitochondrial intermembrane space (Jastroch et al., 2010). While we did not detect guanosine diphosphate (GDP), we noted that both 5'-GMP (guanosine monophosphate) and its precursor guanosine gained *de novo* oscillation on HFD and showed a massive increase during the light phase, peaking at ZT8 (**Figures 7B** and **7C**). BAT contains high levels of GMP reductase (GMPr), which catalyzes the reductive deamination of guanine nucleotides to inosine monophosphate (IMP), thus facilitating the activation of UCP1 by releasing endogenous inhibition by these nucleotides. IMP can be further converted to AMP and dephosphorylated to form adenosine, an activator of brown adipocytes (Gnad et al., 2014). In agreement with increased 5'-GMP, IMP, AMP, and adenosine were all increased in BAT from HFD mice, with a gradual reduction across the circadian cycle depending on their metabolic vicinity to GMP (**Figures 7B** and **7C**).

Due to their important roles in metabolic regulation and signaling, intracellular concentrations of purine nucleotides are normally kept under tight control by continuous inter-conversion and catabolism (Bender, 2011). Degradation can follow alternate routes (**Figure 7D**), mostly relying on reduction of nicotinamide adenine dinucleotide (NAD<sup>+</sup>) to NADH, including conversion of IMP to xanthosine monophosphate (XMP) via IMP dehydrogenase (IMPDH), conversion of hypoxanthine to xanthine, and conversion of xanthine to uric acid via xanthine dehydrogenase (XDH). The XDH enzyme is also inter-convertible with xanthine oxidase (XO), which transfers electrons from xanthine to oxygen instead of NAD<sup>+</sup>, and produces superoxide anion and hydrogen peroxide rather than NADH (Nishino et al., 2008). Interestingly, similar to the liver (Eckel-Mahan et al., 2013), 24-hr NAD<sup>+</sup> oscillation was abolished in BAT on HFD, with NAD<sup>+</sup> at constitutively low levels (**Figure 7E**), supporting a scenario of impaired BAT purine nucleotide catabolism on HFD.

NAD<sup>+</sup> provides metabolic regulation in both mitochondrial and nuclear pools (Mori et al., 2005; Scher et al., 2007). Similarly, nicotinamide (NAM), produced from SIRT3 deacetylase activity and precursor for NAD<sup>+</sup> salvage via nicotinamide phosphoribosyltransferase (NAMPT), also lost oscillation on HFD (**Figure 7E**). Finally, 24-hr oscillation of hypoxanthine, xanthine, and allantoin were all severely blunted in BAT on HFD (**Figure 7F**), further suggesting reduced purine catabolism.

*Sirt3* and *Nampt* are direct BMAL1 targets (Koike et al., 2012; Nakahata et al., 2009; Rey et al., 2011). Thus, HFD-induced attenuation of BAT clock function may directly impair *Sirt3* and *Nampt* expression. Indeed, clock genes *Bmal1* and *Clock* showed altered expression on HFD (**Figure S4A**). Also, *Nampt* and *Sirt3* showed altered 24-hr expression profiles (**Figure S4B**); however, *Nampt* showed modestly reduced expression during

(D) Scheme showing how metabolites of BAT purine catabolism are interrelated and altered on HFD. Metabolites significantly increased by HFD are indicated by red text, while significantly reduced metabolites are blue. Black metabolites are unchanged, and gray metabolites were not measured. Enzymes are shown as pink boxes and are all coded by circadian genes in BAT.

(E) Diurnal variations of NAD<sup>+</sup> metabolites (mean  $\pm$  SEM; n = 5  $\times$  group  $\times$  time point). *Nampt* and *Sirt3* are coded by circadian genes in BAT.

(F) Diurnal variations of selected purine catabolism metabolites in BAT (mean  $\pm$  SEM; n = 5  $\times$  group  $\times$  time point).

(G) Respiration-driving proton leak measured in isolated mitochondria from control HEK293 cells (empty, left) or HEK293 cells ectopically expressing mouse UCP1 (middle) in the presence of selected purine nucleotides. Note that the upward shift in leak kinetics in the presence of UCP1 is prevented to a similar extent by GDP and GMP addition. Right: Data plotted at the highest common membrane potential.

the light phase, while *Sirt3* was significantly increased during the dark phase. Additional circadian genes in BAT, such as *Gmpr* (coding for GMP reductase), *Impdh1* (coding for IMP dehydrogenase), and *Ucp1*, also showed drastic alterations on HFD (Figures S4B and S4C). It is thus plausible that altered 24-hr profiles of many BAT metabolites on HFD may reflect functional defects linked to local clock disruption and misalignment.

Accumulation of purine nucleotides in the absence of activating fatty acids results in UCP1 inhibition and reduced BAT-derived energy expenditure, but the significance of ~7- to 8-fold increased GMP levels in BAT on HFD (Figure 7B) is unclear due to its 50-fold lower binding affinity for UCP1 (Klin- genberg and Huang, 1999). Endogenous levels of GMP and GDP in BAT are unknown, but 120–130 uM GMP and 50 uM GDP has been reported in mouse heart (McKee et al., 1999) and ~20-fold differences of GMP concentration in whole cell (~100 uM) versus mitochondrial matrix (~4 uM) of HeLa cells (Chen et al., 2016). To investigate the role of GMP and IMP per se in driving proton leak inhibition, we utilized isolated mitochondria from stable human embryonic kidney cells (HEK293) ectopically expressing mouse UCP1 (Hirschberg et al., 2011). Importantly, mouse UCP1 displays native behavior in this system (i.e., fatty acid and GDP sensitivity) without inducing artificial uncoupling. Addition of purines GDP, GMP, or IMP to mitochondria from control HEK293 cells had no effect on respiration driving proton leak (Figure 7G). However, in presence of UCP1, there was an upward shift in the proton leak kinetics (relationship between respiration rate and membrane potential), indicating increased uncoupling (Divakaruni and Brand, 2011), which was prevented to a similar extent after addition of GDP or GMP. At the highest common membrane potential, addition of GMP or GDP to UCP1-containing mitochondria caused a similar decrease in proton conductance (Figure 7G), while addition of IMP had no effect on respiration rate or membrane potential. This indicates the importance of a guanine moiety for UCP1 inhibition. Altogether, our data suggest that increased GMP in BAT on HFD is physiologically relevant and may be sufficient to significantly impair proton leak, especially within the context of drastically reduced fatty acid levels on HFD (Figure 7A). This would severely reduce BAT contribution to global energy expenditure and promote expansion and accumulation of lipid stores.

## DISCUSSION

Homeostasis is maintained by coordinating physiological responses among organs and tissues (Roenneberg and Merrow, 2016). While circadian clocks are known to play various homeostatic roles (Eckel-Mahan and Sassone-Corsi, 2013), understanding how 24-hr metabolism is coordinated among various tissue clocks has remained limited. Our study provides a comprehensive map of both temporal and spatial distribution of metabolites over 24 hr and reveals intra- and inter-tissue relationships under conditions of energy balance and imbalance. We uncover how metabolites are linked within and across various tissues over time and how these connections are modified by nutrient stress. This uniquely systems-level view of how tissue metabolism is organized over time has the potential to reveal

previously unappreciated metabolic relationships ripe for therapeutic exploitation.

For example, increased blood concentration of specific amino acids and their metabolites is associated with obesity and type 2 diabetes mellitus (T2DM) (Adams, 2011; Adibi, 1968; Felig et al., 1969). While BCAs are predictive biomarkers for T2D risk (Batch et al., 2013; Newgard, 2009, 2012; Wang et al., 2011), their origin is debatable (Herman et al., 2010; Herrero et al., 1997; Zhao et al., 2016). Our data support a scenario where increased circulating amino acids mostly reflect increased skeletal muscle protein turnover (Figures 6A and S3). Increased circulating levels of alanine and glutamine on HFD most likely originate from muscle proteolysis and metabolism of BCAA, with increased release of BCKA. Our atlas suggests further investigation of serum alanine as a biomarker for T2DM and cardiovascular disease risk is warranted, in keeping with findings on alanine aminotransferase (ALT) (Vozarova et al., 2002; Zhou et al., 2013) and recent indications in human T2DM patients (Isherwood et al., 2017). We thus propose a more general “risk network” of alanine-related metabolites and enzymatic biomarkers.

We also show how loss of BAT metabolite lipid oscillation in conjunction with *de novo* oscillation of purine nucleotides may be relevant for UCP1 function (Figure 7B). The pre-awakening hours (ZT8–ZT10) are particularly important for normal BAT physiology and coincide with the peak of glucose uptake (van der Veen et al., 2012) and REV-ERB $\alpha$  expression, a critical regulator of circadian BAT function (Gerhart-Hines et al., 2013). Human BAT exhibits a similar “dawning” phenomenon, i.e., coupling glucose uptake rhythm to heat production before awakening (Lee et al., 2016), which also coincides with the peak of diurnal plasma catecholamine levels (Scheer et al., 2010). Interestingly, BAT circadian activation appears to be a clock-driven anticipatory process as it persists *ex vivo*, without external cues (Lee et al., 2016).

Loss of NAD $^{+}$  oscillation during the light phase can explain impaired purine nucleotide degradation and may contribute to UCP1 inhibition by increasing GMP levels during this crucial time point. Notably, elevated levels of GMP, IMP, and AMP are observed in erythrocytes from diabetic patients (Dudzinska and Hlynyczak, 2004), and elevated blood purine nucleotides are common pathophysiological consequences of metabolic diseases (Park et al., 2015). Loss of NAD $^{+}$  and NAM oscillations in BAT on HFD may be caused by circadian disruption of enzymes involved in their formation (Eckel-Mahan et al., 2013). Indeed, expression of core clock genes (*Bmal1* and *Clock*) and BAT circadian genes regulating NAD $^{+}$  formation (*Sirt3* and *Nampt*) are altered by HFD (Figures S4A and S4B). Likewise, circadian expression of genes regulating purine nucleotide metabolism (*Impdh1* and *Gmpr*) and thermogenesis (*Ucp1*) were severely impacted by HFD. Thus, BAT circadian function likely involves close coordination between transcriptional regulation and metabolites.

In summary, our atlas constitutes a rich starting point for hypothesis generation and validation by allowing for the temporal reconstruction of complex metabolic networks across tissues and under different feeding paradigms. Additional studies are needed to further elaborate subcellular metabolite localization

and dynamics (Aguilar-Arnal et al., 2016; Aviram et al., 2016; Dyar and Eckel-Mahan, 2017; Mauvoisin et al., 2017) and to monitor inter-organ metabolite fluxes. While a wide range of intra- and inter-tissue metabolite correlations describing potentially novel predictive biomarkers and pathogenic networks remains to be explored, this resource can already serve as a basis for future studies integrating subcellular metabolomics data, clock gene mutants, additional feeding regimes, and exercise protocols.

## STAR★METHODS

Detailed methods are provided in the online version of this paper and include the following:

- KEY RESOURCES TABLE
- CONTACT FOR REAGENT AND RESOURCE SHARING
- EXPERIMENTAL MODEL AND SUBJECT DETAILS
  - Ethics Statement
  - Animals, diets and tissue collection
  - Cell culture
- METHOD DETAILS
  - Global metabolite profiling
  - Metabolomics data processing and analysis
  - Statistical analysis of metabolites
  - Robust Correlations
  - *In vitro* functional characterization of proton leak kinetics
  - BAT qPCR
- QUANTIFICATION AND STATISTICAL ANALYSIS
- DATA AVAILABILITY

## SUPPLEMENTAL INFORMATION

Supplemental Information includes four figures and six tables and can be found with this article online at <https://doi.org/10.1016/j.cell.2018.08.042>.

## ACKNOWLEDGMENTS

This work was supported by NIH grant GM123558 and DARPA grant D17AP00002 (P.B.); DFG Emmy Noether NHU 275/1-1 (N.H.U.); the Alexander von Humboldt Foundation (M.H.T.); NIH DK114037 (K.E.M.); by INSERM (Institut National de la Santé et de la Recherche Médicale, France), KAUST (King Abdullah University of Science and Technology), National Institutes of Health, and Novo Nordisk Foundation Challenge Grant NNF140C0011493 (P.S.-C.); and by the German Federal Ministry of Education and Research (BMBF) to the German Center Diabetes Research (DZD e.V.) grant to J.A.

## AUTHOR CONTRIBUTIONS

Conceptualization, K.A.D., K.E.-M., P.S.-C., J.A., S.d.M., and M.H.T.; Methodology, K.A.D., D.L., A.A., N.J.C., Y.L., D.A., S.S., S.d.M., S.A., P.T., R.O.-S., K.K., P.B., J.A., and K.E.-M.; Investigation, K.A.D., D.L., A.A., N.J.C., Y.L., D.A., M.J., S.S., M.C., S.d.M., S.A., P.T., R.O.-S., K.K., S.N., J.A., and K.E.-M.; Data Analysis, K.A.D., D.L., A.A., N.J.C., Y.L., D.A., M.J., S.S., S.d.M., M.C., S.A., P.T., R.O.-S., K.K., J.A., K.E.-M., M.H.T., and P.S.-C.; Writing – Review & Editing, K.A.D., D.L., K.E.-M., M.J., J.A., E.B., S.M., M.H.T., and P.S.-C.; Funding Acquisition, P.S.-C., M.H.T., N.H.U., V.O., and P.M.; Resources: D.L., A.A., N.J.C., Y.L., D.A., C.W., R.S., V.O., P.B., J.A., M.H.T., and P.S.-C.; Supervision, C.W., R.S., N.H.U., P.M., V.O., P.B., J.A., M.H.T., and P.S.-C.

## DECLARATION OF INTERESTS

The authors declare no competing interests.

Received: March 20, 2018  
Revised: May 20, 2018  
Accepted: August 20, 2018  
Published: September 6, 2018

## REFERENCES

- Abbondante, S., Eckel-Mahan, K.L., Ceglia, N.J., Baldi, P., and Sassone-Corsi, P. (2016). Comparative circadian metabolomics reveal differential effects of nutritional challenge in the serum and liver. *J. Biol. Chem.* **291**, 2812–2828.
- Adams, S.H. (2011). Emerging perspectives on essential amino acid metabolism in obesity and the insulin-resistant state. *Adv. Nutr.* **2**, 445–456.
- Adibi, S.A. (1968). Influence of dietary deprivations on plasma concentration of free amino acids of man. *J. Appl. Physiol.* **25**, 52–57.
- Agostinelli, F., Ceglia, N., Shahbaba, B., Sassone-Corsi, P., and Baldi, P. (2016). What time is it? Deep learning approaches for circadian rhythms. *Bioinformatics* **32**, i8–i17.
- Aguilar-Arnal, L., Ranjit, S., Stringari, C., Orozco-Solis, R., Gratton, E., and Sassone-Corsi, P. (2016). Spatial dynamics of SIRT1 and the subnuclear distribution of NADH species. *Proc. Natl. Acad. Sci. USA*, 201609227.
- Asher, G., and Sassone-Corsi, P. (2015). Time for food: the intimate interplay between nutrition, metabolism, and the circadian clock. *Cell* **161**, 84–92.
- Aviram, R., Manella, G., Kopelman, N., Neufeld-Cohen, A., Zwighart, Z., Elimelech, M., Adamovich, Y., Golik, M., Wang, C., Han, X., and Asher, G. (2016). Lipidomics analyses reveal temporal and spatial lipid organization and uncover daily oscillations in intracellular organelles. *Mol. Cell* **62**, 636–648.
- Batch, B.C., Shah, S.H., Newgard, C.B., Turer, C.B., Haynes, C., Bain, J.R., Muehlbauer, M., Patel, M.J., Stevens, R.D., Appel, L.J., et al. (2013). Branched chain amino acids are novel biomarkers for discrimination of metabolic wellness. *Metabolism* **62**, 961–969.
- Bender, D. (2011). *Amino Acid Metabolism*, Third Edition (Wiley-Blackwell).
- Brown, S.A. (2016). Circadian metabolism: from mechanisms to metabolomics and medicine. *Trends Endocrinol. Metab.* **27**, 415–426.
- Chen, W.W., Freinkman, E., Wang, T., Birsoy, K., and Sabatini, D.M. (2016). Absolute quantification of matrix metabolites reveals the dynamics of mitochondrial metabolism. *Cell* **166**, 1324–1337.e1311.
- Dallmann, R., Viola, A.U., Tarokh, L., Cajochen, C., and Brown, S.A. (2012). The human circadian metabolome. *Proc. Natl. Acad. Sci. USA* **109**, 2625–2629.
- Davies, S.K., Ang, J.E., Revell, V.L., Holmes, B., Mann, A., Robertson, F.P., Cui, N., Middleton, B., Ackermann, K., Kayser, M., et al. (2014). Effect of sleep deprivation on the human metabolome. *Proc. Natl. Acad. Sci. USA* **111**, 10761–10766.
- DeBerardinis, R.J., and Thompson, C.B. (2012). Cellular metabolism and disease: what do metabolic outliers teach us? *Cell* **148**, 1132–1144.
- Divakaruni, A.S., and Brand, M.D. (2011). The regulation and physiology of mitochondrial proton leak. *Physiology (Bethesda)* **26**, 192–205.
- Dudzinska, W., and Hlynyczak, A.J. (2004). Purine nucleotides and their metabolites in erythrocytes of streptozotocin diabetic rats. *Diabetes Metab.* **30**, 557–567.
- Dunford, E.C., and Riddell, M.C. (2016). The metabolic implications of glucocorticoids in a high-fat diet setting and the counter-effects of exercise. *Metabolites* **6**, E44.
- Dyar, K.A., Ciciliot, S., Wright, L.E., Biensø, R.S., Tagliazucchi, G.M., Patel, V.R., Forcato, M., Paz, M.I., Gudiksen, A., Solagna, F., et al. (2013). Muscle insulin sensitivity and glucose metabolism are controlled by the intrinsic muscle clock. *Mol. Metab.* **3**, 29–41.
- Dyar, K.A., and Eckel-Mahan, K.L. (2017). Circadian metabolomics in time and space. *Front. Neurosci.* **11**, 369.

- Eckel, R.H., Grundy, S.M., and Zimmet, P.Z. (2005). The metabolic syndrome. *Lancet* 365, 1415–1428.
- Eckel-Mahan, K., and Sassone-Corsi, P. (2013). Metabolism and the circadian clock converge. *Physiol. Rev.* 93, 107–135.
- Eckel-Mahan, K.L., Patel, V.R., de Mateo, S., Orozco-Solis, R., Ceglia, N.J., Sahar, S., Dilag-Penilla, S.A., Dyer, K.A., Baldi, P., and Sassone-Corsi, P. (2013). Reprogramming of the circadian clock by nutritional challenge. *Cell* 155, 1464–1478.
- Eckel-Mahan, K.L., Patel, V.R., Mohney, R.P., Vignola, K.S., Baldi, P., and Sassone-Corsi, P. (2012). Coordination of the transcriptome and metabolome by the circadian clock. *Proc. Natl. Acad. Sci. USA* 109, 5541–5546.
- Elia, M., Carter, A., Bacon, S., Winearls, C.G., and Smith, R. (1981). Clinical usefulness of urinary 3-methylhistidine excretion in indicating muscle protein breakdown. *Br. Med. J. (Clin. Res. Ed.)* 282, 351–354.
- Felig, P. (1973). The glucose-alanine cycle. *Metabolism* 22, 179–207.
- Felig, P., Marliss, E., and Cahill, G.F., Jr. (1969). Plasma amino acid levels and insulin secretion in obesity. *N. Engl. J. Med.* 281, 811–816.
- Fustin, J.M., Doi, M., Yamada, H., Komatsu, R., Shimba, S., and Okamura, H. (2012). Rhythmic nucleotide synthesis in the liver: temporal segregation of metabolites. *Cell Rep.* 1, 341–349.
- Gerhart-Hines, Z., Feng, D., Emmett, M.J., Everett, L.J., Loro, E., Briggs, E.R., Bugge, A., Hou, C., Ferrara, C., Seale, P., et al. (2013). The nuclear receptor Rev-erb $\alpha$  controls circadian thermogenic plasticity. *Nature* 503, 410–413.
- German, J.B., Hammock, B.D., and Watkins, S.M. (2005). Metabolomics: building on a century of biochemistry to guide human health. *Metabolomics* 1, 3–9.
- Giskeødegård, G.F., Davies, S.K., Revell, V.L., Keun, H., and Skene, D.J. (2015). Diurnal rhythms in the human urine metabolome during sleep and total sleep deprivation. *Sci. Rep.* 5, 14843.
- Gnad, T., Scheibler, S., von Kügelgen, I., Scheele, C., Kilić, A., Glöde, A., Hoffmann, L.S., Reverte-Salisa, L., Horn, P., Mutlu, S., et al. (2014). Adenosine activates brown adipose tissue and recruits beige adipocytes via A2A receptors. *Nature* 516, 395–399.
- Goodacre, R. (2007). Metabolomics of a superorganism. *J. Nutr.* 137(1, Suppl), 259S–266S.
- Gooley, J.J., and Chua, E.C. (2014). Diurnal regulation of lipid metabolism and applications of circadian lipidomics. *J. Genet. Genomics* 41, 231–250.
- Guggenheim, K.Y. (1991). Rudolf Schoenheimer and the concept of the dynamic state of body constituents. *J. Nutr.* 121, 1701–1704.
- Hatting, M., Tavares, C.D.J., Sharabi, K., Rines, A.K., and Puigserver, P. (2018). Insulin regulation of gluconeogenesis. *Ann. N Y Acad. Sci.* 1411, 21–35.
- Herman, M.A., She, P., Peroni, O.D., Lynch, C.J., and Kahn, B.B. (2010). Adipose tissue branched chain amino acid (BCAA) metabolism modulates circulating BCAA levels. *J. Biol. Chem.* 285, 11348–11356.
- Herrero, M.C., Remesar, X., Bladé, C., and Arola, L. (1997). Muscle amino acid pattern in obese rats. *Int. J. Obes. Relat. Metab. Disord.* 21, 698–703.
- Hirschberg, V., Fromme, T., and Klingenspor, M. (2011). Test systems to study the structure and function of uncoupling protein 1: a critical overview. *Front. Endocrinol. (Lausanne)* 2, 63.
- Hughes, M.E., Hogenesch, J.B., and Kornacker, K. (2010). JTK\_CYCLE: an efficient nonparametric algorithm for detecting rhythmic components in genome-scale data sets. *J. Biol. Rhythms* 25, 372–380.
- Isherwood, C.M., Van der Veen, D.R., Johnston, J.D., and Skene, D.J. (2017). Twenty-four-hour rhythmicity of circulating metabolites: effect of body mass and type 2 diabetes. *FASEB J.* 31, 5557–5567.
- Jastroch, M. (2012). Expression of uncoupling proteins in a mammalian cell culture system (HEK293) and assessment of their protein function. *Methods Mol. Biol.* 810, 153–164.
- Jastroch, M., Divakaruni, A.S., Mookerjee, S., Treberg, J.R., and Brand, M.D. (2010). Mitochondrial proton and electron leaks. *Essays Biochem.* 47, 53–67.
- Jastroch, M., Hirschberg, V., and Klingenspor, M. (2012). Functional characterization of UCP1 in mammalian HEK293 cells excludes mitochondrial uncoupling artefacts and reveals no contribution to basal proton leak. *Biochim. Biophys. Acta* 1817, 1660–1670.
- Jouffe, C., Gobet, C., Martin, E., Métairon, S., Morin-Rivron, D., Masoodi, M., and Gachon, F. (2016). Perturbed rhythmic activation of signaling pathways in mice deficient for Sterol Carrier Protein 2-dependent diurnal lipid transport and metabolism. *Sci. Rep.* 6, 24631.
- Kim, K., Mall, C., Taylor, S.L., Hitchcock, S., Zhang, C., Wettersten, H.I., Jones, A.D., Chapman, A., and Weiss, R.H. (2014). Mealtime, temporal, and daily variability of the human urinary and plasma metabolomes in a tightly controlled environment. *PLoS ONE* 9, e86223.
- Klingenberg, M., and Huang, S.G. (1999). Structure and function of the uncoupling protein from brown adipose tissue. *Biochim. Biophys. Acta* 1415, 271–296.
- Koike, N., Yoo, S.H., Huang, H.C., Kumar, V., Lee, C., Kim, T.K., and Takahashi, J.S. (2012). Transcriptional architecture and chromatin landscape of the core circadian clock in mammals. *Science* 338, 349–354.
- Krishnaiah, S.Y., Wu, G., Altman, B.J., Growe, J., Rhoades, S.D., Coldren, F., Venkataraman, A., Olarerin-George, A.O., Francey, L.J., Mukherjee, S., et al. (2017). Clock regulation of metabolites reveals coupling between transcription and metabolism. *Cell Metab* 25, 961–974.e964.
- Lee, P., Bova, R., Schofield, L., Bryant, W., Dieckmann, W., Slattery, A., Govendir, M.A., Emmett, L., and Greenfield, J.R. (2016). Brown adipose tissue exhibits a glucose-responsive thermogenic biorhythm in humans. *Cell Metab.* 23, 602–609.
- Lowrey, P.L., and Takahashi, J.S. (2011). Genetics of circadian rhythms in Mammalian model organisms. *Adv. Genet.* 74, 175–230.
- Lu, X., Solmonson, A., Lodi, A., Nowinski, S.M., Sentandreu, E., Riley, C.L., Mills, E.M., and Tiziani, S. (2017). The early metabolomic response of adipose tissue during acute cold exposure in mice. *Sci. Rep.* 7, 3455.
- Martinez-Lozano Sinues, P., Tarokh, L., Li, X., Kohler, M., Brown, S.A., Zenobi, R., and Dallmann, R. (2014). Circadian variation of the human metabolome captured by real-time breath analysis. *PLoS ONE* 9, e114422.
- Masri, S., Rigor, P., Cervantes, M., Ceglia, N., Sebastian, C., Xiao, C., Roqueta-Rivera, M., Deng, C., Osborne, T.F., Mostoslavsky, R., et al. (2014). Partitioning circadian transcription by SIRT6 leads to segregated control of cellular metabolism. *Cell* 158, 659–672.
- Mauvoisin, D., Atger, F., Dayon, L., Núñez Galindo, A., Wang, J., Martin, E., Da Silva, L., Montoliu, I., Collino, S., Martin, F.P., et al. (2017). Circadian and feeding rhythms orchestrate the diurnal liver acetylome. *Cell Rep.* 20, 1729–1743.
- McKee, E.E., Bentley, A.T., Smith, R.M., Jr., and Ciaccio, C.E. (1999). Origin of guanine nucleotides in isolated heart mitochondria. *Biochem. Biophys. Res. Commun.* 257, 466–472.
- Mori, S., Kawai, S., Shi, F., Mikami, B., and Murata, K. (2005). Molecular conversion of NAD kinase to NADH kinase through single amino acid residue substitution. *J. Biol. Chem.* 280, 24104–24112.
- Nakahata, Y., Sahar, S., Astarita, G., Kaluzova, M., and Sassone-Corsi, P. (2009). Circadian control of the NAD $^{+}$  salvage pathway by CLOCK-SIRT1. *Science* 324, 654–657.
- Newgard, C.B. (2012). Interplay between lipids and branched-chain amino acids in development of insulin resistance. *Cell Metab.* 15, 606–614.
- Newgard, C.B., An, J., Bain, J.R., Muehlbauer, M.J., Stevens, R.D., Lien, L.F., Haqq, A.M., Shah, S.H., Ariotto, M., Sletz, C.A., et al. (2009). A branched-chain amino acid-related metabolic signature that differentiates obese and lean humans and contributes to insulin resistance. *Cell Metab.* 9, 311–326.
- Nicholls, D.G., and Locke, R.M. (1984). Thermogenic mechanisms in brown fat. *Physiol. Rev.* 64, 1–64.
- Nishino, T., Okamoto, K., Eger, B.T., Pai, E.F., and Nishino, T. (2008). Mammalian xanthine oxidoreductase - mechanism of transition from xanthine dehydrogenase to xanthine oxidase. *FEBS J.* 275, 3278–3289.
- Noguchi, R., Kubota, H., Yugi, K., Toyoshima, Y., Komori, Y., Soga, T., and Kuroda, S. (2013). The selective control of glycolysis, gluconeogenesis and glycogenesis by temporal insulin patterns. *Mol. Syst. Biol.* 9, 664.

- Nye, C., Kim, J., Kalhan, S.C., and Hanson, R.W. (2008). Reassessing triglyceride synthesis in adipose tissue. *Trends Endocrinol. Metab.* 19, 356–361.
- O'Neill, J.S., Maywood, E.S., Chesham, J.E., Takahashi, J.S., and Hastings, M.H. (2008). cAMP-dependent signaling as a core component of the mammalian circadian pacemaker. *Science* 320, 949–953.
- O'Neill, J.S., van Ooijen, G., Dixon, L.E., Troein, C., Corellou, F., Bouget, F.Y., Reddy, A.B., and Millar, A.J. (2011). Circadian rhythms persist without transcription in a eukaryote. *Nature* 469, 554–558.
- Oakes, N.D., Bell, K.S., Furler, S.M., Camilleri, S., Saha, A.K., Ruderman, N.B., Chisholm, D.J., and Kraegen, E.W. (1997). Diet-induced muscle insulin resistance in rats is ameliorated by acute dietary lipid withdrawal or a single bout of exercise: parallel relationship between insulin stimulation of glucose uptake and suppression of long-chain fatty acyl-CoA. *Diabetes* 46, 2022–2028.
- Odessey, R., and Goldberg, A.L. (1979). Leucine degradation in cell-free extracts of skeletal muscle. *Biochem. J.* 178, 475–489.
- Park, S., Sadanala, K.C., and Kim, E.K. (2015). A metabolomic approach to understanding the metabolic link between obesity and diabetes. *Mol. Cells* 38, 587–596.
- Patel, V.R., Eckel-Mahan, K., Sassone-Corsi, P., and Baldi, P. (2012). CircadiOmics: integrating circadian genomics, transcriptomics, proteomics and metabolomics. *Nat. Methods* 9, 772–773.
- Peek, C.B., Affinati, A.H., Ramsey, K.M., Kuo, H.Y., Yu, W., Sena, L.A., Ilkayeva, O., Marcheva, B., Kobayashi, Y., Omura, C., et al. (2013). Circadian clock NAD<sup>+</sup> cycle drives mitochondrial oxidative metabolism in mice. *Science* 342, 1243417.
- Pozefsky, T., Felig, P., Tobin, J.D., Soeldner, J.S., and Cahill, G.F., Jr. (1969). Amino acid balance across tissues of the forearm in postabsorptive man. Effects of insulin at two dose levels. *J. Clin. Invest.* 48, 2273–2282.
- Ramsey, K.M., Yoshino, J., Brace, C.S., Abrassart, D., Kobayashi, Y., Marcheva, B., Hong, H.K., Chong, J.L., Buhr, E.D., Lee, C., et al. (2009). Circadian clock feedback cycle through NAMPT-mediated NAD<sup>+</sup> biosynthesis. *Science* 324, 651–654.
- Rey, G., Cesbron, F., Rougemont, J., Reinke, H., Brunner, M., and Naef, F. (2011). Genome-wide and phase-specific DNA-binding rhythms of BMAL1 control circadian output functions in mouse liver. *PLoS Biol.* 9, e1000595.
- Rey, G., Valekunja, U.K., Feeney, K.A., Wulund, L., Milev, N.B., Stangerlin, A., Ansel-Bollepalli, L., Velagapudi, V., O'Neill, J.S., and Reddy, A.B. (2016). The pentose phosphate pathway regulates the circadian clock. *Cell Metab.* 24, 462–473.
- Roenneberg, T., Allebrandt, K.V., Merrow, M., and Vetter, C. (2012). Social jet-lag and obesity. *Curr. Biol.* 22, 939–943.
- Roenneberg, T., and Merrow, M. (2016). The circadian clock and human health. *Curr. Biol.* 26, R432–R443.
- Roseno, S.L., Davis, P.R., Bollinger, L.M., Powell, J.J., Witczak, C.A., and Brault, J.J. (2015). Short-term, high-fat diet accelerates disuse atrophy and protein degradation in a muscle-specific manner in mice. *Nutr. Metab. (Lond.)* 12, 39.
- Scheer, F.A., Hu, K., Evoniuk, H., Kelly, E.E., Malhotra, A., Hilton, M.F., and Shea, S.A. (2010). Impact of the human circadian system, exercise, and their interaction on cardiovascular function. *Proc. Natl. Acad. Sci. USA* 107, 20541–20546.
- Scher, M.B., Vaquero, A., and Reinberg, D. (2007). SirT3 is a nuclear NAD<sup>+</sup>-dependent histone deacetylase that translocates to the mitochondria upon cellular stress. *Genes Dev.* 21, 920–928.
- Schiaffino, S., Dyer, K.A., Ciccioli, S., Blaauw, B., and Sandri, M. (2013). Mechanisms regulating skeletal muscle growth and atrophy. *FEBS J.* 280, 4294–4314.
- Serra, F., Gianotti, M., Pons, A., and Palou, A. (1994). Brown and white adipose tissue adaptive enzymatic changes on amino acid metabolism in persistent dietary-obese rats. *Biochem. Mol. Biol. Int.* 32, 1173–1178.
- Shabalina, I.G., Jacobsson, A., Cannon, B., and Nedergaard, J. (2004). Native UCP1 displays simple competitive kinetics between the regulators purine nucleotides and fatty acids. *J. Biol. Chem.* 279, 38236–38248.
- Shimizu, N., Maruyama, T., Yoshikawa, N., Matsumiya, R., Ma, Y., Ito, N., Tasaka, Y., Kuribara-Souta, A., Miyata, K., Oike, Y., et al. (2015). A muscle-liver-fat signalling axis is essential for central control of adaptive adipose remodeling. *Nat. Commun.* 6, 6693.
- Shin, S.Y., Fauman, E.B., Petersen, A.K., Krumsiek, J., Santos, R., Huang, J., Arnold, M., Erte, I., Forgetta, V., Yang, T.P., et al.; Multiple Tissue Human Expression Resource (MuTHER) Consortium (2014). An atlas of genetic influences on human blood metabolites. *Nat. Genet.* 46, 543–550.
- Sishi, B., Loos, B., Ellis, B., Smith, W., du Toit, E.F., and Engelbrecht, A.M. (2011). Diet-induced obesity alters signalling pathways and induces atrophy and apoptosis in skeletal muscle in a prediabetic rat model. *Exp. Physiol.* 96, 179–193.
- Snell, K., and Duff, D.A. (1979). Muscle phosphoenolpyruvate carboxykinase activity and alanine release in progressively starved rats. *Int. J. Biochem.* 10, 423–426.
- Song, S., Andrikopoulos, S., Filippis, C., Thorburn, A.W., Khan, D., and Proietto, J. (2001). Mechanism of fat-induced hepatic gluconeogenesis: effect of metformin. *Am. J. Physiol. Endocrinol. Metab.* 281, E275–E282.
- Sugimoto, M., Ikeda, S., Niigata, K., Tomita, M., Sato, H., and Soga, T. (2012). MMMDB: Mouse Multiple Tissue Metabolome Database. *Nucleic Acids Res.* 40, D809–D814.
- Tu, B.P., and McKnight, S.L. (2006). Metabolic cycles as an underlying basis of biological oscillations. *Nat. Rev. Mol. Cell Biol.* 7, 696–701.
- van der Veen, D.R., Shao, J., Chapman, S., Leevy, W.M., and Duffield, G.E. (2012). A diurnal rhythm in glucose uptake in brown adipose tissue revealed by *in vivo* PET-FDG imaging. *Obesity (Silver Spring)* 20, 1527–1529.
- Vozarova, B., Stefan, N., Lindsay, R.S., Saremi, A., Pratley, R.E., Bogardus, C., and Tataranni, P.A. (2002). High alanine aminotransferase is associated with decreased hepatic insulin sensitivity and predicts the development of type 2 diabetes. *Diabetes* 51, 1889–1895.
- Wang, T.J., Larson, M.G., Vasan, R.S., Cheng, S., Rhee, E.P., McCabe, E., Lewis, G.D., Fox, C.S., Jacques, P.F., Fernandez, C., et al. (2011). Metabolite profiles and the risk of developing diabetes. *Nat. Med.* 17, 448–453.
- Xia, J., and Wishart, D.S. (2016). Using MetaboAnalyst 3.0 for comprehensive metabolomics data analysis. *Curr. Protoc. Bioinformatics* 55, 14.10.11–14.10.91.
- Zhang, S., Hulver, M.W., McMillan, R.P., Cline, M.A., and Gilbert, E.R. (2014). The pivotal role of pyruvate dehydrogenase kinases in metabolic flexibility. *Nutr. Metab. (Lond.)* 11, 10.
- Zhao, X., Han, Q., Liu, Y., Sun, C., Gang, X., and Wang, G. (2016). The relationship between branched-chain amino acid related metabolomic signature and insulin resistance: a systematic review. *J. Diabetes Res.* 2016, 2794591.
- Zhou, J., Mo, Y., Li, H., Ran, X., Yang, W., Li, Q., Peng, Y., Li, Y., Gao, X., Luan, X., et al. (2013). Alanine aminotransferase is associated with an adverse nocturnal blood glucose profile in individuals with normal glucose regulation. *PLoS ONE* 8, e56072.
- Zwighaft, Z., Aviram, R., Shalev, M., Rousso-Noori, L., Kraut-Cohen, J., Golik, M., Brandis, A., Reinke, H., Aharoni, A., Kahana, C., and Asher, G. (2015). Circadian clock control by polyamine levels through a mechanism that declines with age. *Cell Metab.* 22, 874–885.

## STAR★METHODS

## KEY RESOURCES TABLE

REAGENT or RESOURCE	SOURCE	IDENTIFIER
<b>Antibodies</b>		
rabbit anti-UCP1 polyclonal antibody	Chemicon	#3046; RRID: AB_2213936
<b>Chemicals, Peptides, and Recombinant Proteins</b>		
TRIzol reagent	Invitrogen	15596018
SsoAdvanced Universal SYBR Green	Bio-Rad	Cat#4385618
iScript cDNA reverse transcription kit	Bio-Rad	Cat#1708891
DMEM, 4,500 mg/L glucose, + L- glutamine, -pyruvate	GIBCO	11965092
FBS	Biochrom	S0115
Gentamycin	GIBCO	15750060
Amphotericin B	Sigma	A2942
Superfect Transfection Reagent	QIAGEN	301305
Geneticin	GIBCO	10131035
Fat-free BSA	Sigma	A3803
GDP	Sigma	G7127
GMP	Sigma	G8377
IMP	Sigma	I4375
<b>Deposited Data</b>		
Mouse brown adipose, high fat diet	<a href="http://circadiomics.ics.uci.edu/">http://circadiomics.ics.uci.edu/</a>	MOUSE BROWN ADIPOSE DYAR 2018 HIGH-FAT
Mouse brown adipose, normal chow	<a href="http://circadiomics.ics.uci.edu/">http://circadiomics.ics.uci.edu/</a>	MOUSE BROWN ADIPOSE DYAR 2018 NORMAL-CHOW
Mouse liver, high fat diet	<a href="http://circadiomics.ics.uci.edu/">http://circadiomics.ics.uci.edu/</a>	MOUSE LIVER METABOLOME ECKEL-MAHAN 2013 HIGH-FAT
Mouse liver, normal chow	<a href="http://circadiomics.ics.uci.edu/">http://circadiomics.ics.uci.edu/</a>	MOUSE LIVER METABOLOME ECKEL-MAHAN 2013 NORMAL-CHOW
Mouse muscle, high fat diet	<a href="http://circadiomics.ics.uci.edu/">http://circadiomics.ics.uci.edu/</a>	MOUSE MUSCLE DYAR 2018 HIGH-FAT
Mouse muscle, normal chow	<a href="http://circadiomics.ics.uci.edu/">http://circadiomics.ics.uci.edu/</a>	MOUSE MUSCLE DYAR 2018 NORMAL-CHOW
Mouse prefrontal cortex, high fat diet	<a href="http://circadiomics.ics.uci.edu/">http://circadiomics.ics.uci.edu/</a>	MOUSE PREFRONTAL CORTEX NA 2018 HIGH-FAT
Mouse prefrontal cortex, normal chow	<a href="http://circadiomics.ics.uci.edu/">http://circadiomics.ics.uci.edu/</a>	MOUSE PREFRONTAL CORTEX NA 2018 NORMAL-CHOW
Mouse serum, high fat diet	<a href="http://circadiomics.ics.uci.edu/">http://circadiomics.ics.uci.edu/</a>	MOUSE SERUM ABBONDANTE 2016 HIGH-FAT
Mouse serum, normal chow	<a href="http://circadiomics.ics.uci.edu/">http://circadiomics.ics.uci.edu/</a>	MOUSE SERUM ABBONDANTE 2016 NORMAL-CHOW
Mouse sperm, high fat diet	<a href="http://circadiomics.ics.uci.edu/">http://circadiomics.ics.uci.edu/</a>	MOUSE SPERM DYAR 2018 HIGH-FAT
Mouse sperm, normal chow	<a href="http://circadiomics.ics.uci.edu/">http://circadiomics.ics.uci.edu/</a>	MOUSE SPERM DYAR 2018 NORMAL-CHOW
Mouse suprachiasmatic nucleus, high fat diet	<a href="http://circadiomics.ics.uci.edu/">http://circadiomics.ics.uci.edu/</a>	MOUSE SUPRACHIASMATIC NUCLEUS NA 2018 HIGH-FAT
Mouse suprachiasmatic nucleus, normal chow	<a href="http://circadiomics.ics.uci.edu/">http://circadiomics.ics.uci.edu/</a>	MOUSE SUPRACHIASMATIC NUCLEUS NA 2018 NORMAL-CHOW
Mouse white adipose, high fat diet	<a href="http://circadiomics.ics.uci.edu/">http://circadiomics.ics.uci.edu/</a>	MOUSE WHITE ADIPOSE DYAR 2018 HIGH-FAT

(Continued on next page)

**Continued**

REAGENT or RESOURCE	SOURCE	IDENTIFIER
Mouse white adipose, normal chow	<a href="http://circadiomics.ics.uci.edu/">http://circadiomics.ics.uci.edu/</a>	MOUSE WHITE ADIPOSE DYAR 2018 NORMAL-CHOW
Raw "origscale" 24-h metabolomics intensity data from 8 different murine tissues under chow or high fat diet	<a href="https://doi.org/10.17632/zndtmk8xc6.1">https://doi.org/10.17632/zndtmk8xc6.1</a>	Table S4
<b>Experimental Models: Cell Lines</b>		
HEK293	Sigma	85120602
<b>Experimental Models: Organisms/Strains</b>		
C57BL/6J	The Jackson Laboratory	000664
Oligonucleotides		
See Table S6 for qPCR primers	N/A	N/A
<b>Recombinant DNA</b>		
pcDNA3.1	Invitrogen	V79020
Mouse UCP1 ORF (NM009463) cloned into pcDNA3.1	Martin Jastroch	N/A
<b>Software and Algorithms</b>		
MATLAB and Statistics Toolbox R2016b	Mathworks	<a href="https://www.mathworks.com/products/new_products/release2016b.html">https://www.mathworks.com/products/new_products/release2016b.html</a>
JTK_CYCLE	Hughes et al., 2010	<a href="https://github.com/mfcovington/jtk-cycle">https://github.com/mfcovington/jtk-cycle</a>
BIO_CYCLE	Agostinelli et al., 2016	<a href="http://circadiomics.igb.uci.edu/static/downloadables/BioCycle.tar.gz">http://circadiomics.igb.uci.edu/static/downloadables/BioCycle.tar.gz</a>
<b>Other</b>		
Vivarium Chow- Prolab RMH 2500	Lab Supply	5P14
High Fat Diet	Research Diets	D12492

**CONTACT FOR REAGENT AND RESOURCE SHARING**

Further information and requests for resources and reagents should be directed to and will be fulfilled by the Lead Contact, Paolo Sassone-Corsi ([psc@uci.edu](mailto:psc@uci.edu)).

**EXPERIMENTAL MODEL AND SUBJECT DETAILS****Ethics Statement**

All experiments were performed in accordance with the Institutional Animal Care and Use Committee (IACUC) guidelines of the University of California at Irvine in compliance with the Animal Welfare Act and other federal and state statutes and regulations relating to animal experiments.

**Animals, diets and tissue collection**

Six week old male C57BL6/J mice were purchased from JAX / Jackson Labs (Stock Number: 000664). Mice were randomly assigned to experimental groups, maintained on a 12hr light/12hr dark cycle (ZT0 corresponds to lights on and ZT12 to lights off in the animal facility), and fed *ad libitum* for 10 weeks with either standard chow diet (Prolab RMH 2500) or high fat diet (HFD) composed of 60% Kcal from fat (Research Diets, D12492). Body weight was measured weekly. Animals were separated into individual cages 1 week before tissue collection. Five male mice for each time point/diet were used. Tissues were immediately collected after cervical dislocation and stored at -80°C until further processing/analysis. Serum was prepared from an abdominal/thoracic blood sample and stored at -80°C. Sperm was collected after swimming out from the caudal portion of the epididymis in non-capacitating media (MEM without BSA) for 10min at 37°C. Sperm cells were then washed with PBS twice at low centrifugation speed and the sperm pellet was rapidly frozen in liquid nitrogen and stored at -80°C.

**Cell culture**

Human embryonic kidney cells (HEK293) were cultured in Dulbecco's Modified Eagle Medium (4500 mg/l glucose, +L-glutamine, -pyruvate) supplemented with 10% fetal calf serum (Biochrom), 50 µg/ml gentamycin and 2.5 µg/ml amphotericin B at 37°C in a

5% CO<sub>2</sub> humidified incubator as described (Jastroch et al., 2012). To passage, medium was removed and cells washed with PBS, trypsinised (0.2% trypsin), suspended in medium, centrifuged (500 g; 3min), resuspended in growth medium and seeded on new plates.

## METHOD DETAILS

### Global metabolite profiling

Non-targeted metabolite profiling, peak identification, and curation was performed by Metabolon (Durham, NC, USA) and by the Genome Analysis Center (GAC), Helmholtz Zentrum München (Neuherberg, Germany). Liver, serum, and sperm were processed and run by Metabolon on an HD3 system using described methods (Abbondante et al., 2016; Eckel-Mahan et al., 2012). Briefly, this analytical system combines a Linear Ion Trap MS/MS (LTQ XL, Thermo Scientific) coupled with UPLC (Acquity, Waters), and consists of 2 reverse phase (RP)/UPLC-MS/MS methods: 1) with positive ion mode electrospray ionization (ESI) optimized for acidic species, and 2) with negative ion mode ESI optimized for basic species. An additional GC/MS platform for volatile compounds was used in parallel. WAT and BAT samples were processed and run by the GAC on the same analytical system, with the exception of the GC/MS platform, and with curation again performed by Metabolon. Skeletal muscle and brain tissues (SCN & mPFC) were processed and run by Metabolon on their HD4 platform, which runs with High Resolution Accurate Mass (HRAM) MS/MS (QExactive, Thermo Scientific) also coupled with UPLC (Acquity, Waters). Overall, we processed and analyzed a total of 70 tissues each of liver, serum, BAT, and WAT (5 replicates x 2 groups x 7 time points, including additional time point ZT24), and 60 tissues each for SCN, mPFC, gastrocnemius skeletal muscle, and sperm (5 replicates x 2 groups x 6 time points). One biological replicate each from chow-fed SCN at ZT20 and from HFD-fed mPFC at ZT4 were lost during sample processing, leaving 4 remaining replicates each for these particular time points/diets. Two biological replicates from chow-fed mPFC at ZT4 were likewise lost, leaving 3 remaining replicates.

### Metabolomics data processing and analysis

For further analysis, we used raw metabolomic intensity data (“origscale,” Table S4). Data processing closely followed procedures reported in (Shin et al., 2014). Run day correction was performed for each metabolite by setting the run day medians equal to 1. We removed metabolites with more than 50% missing values and transformed data to log<sub>10</sub>. Data points outside 4 times the standard deviation for each metabolite were considered as outliers and removed. Missing data were imputed by k-nearest-neighbor. (Missing Values: 5% BAT, 25% BrainPFC, 5% BrainSCN, 5% Liver, 17% Muscle, 6% Serum, 17% WAT, 8% SCN).

### Statistical analysis of metabolites

Heatmaps were generated using the median of 5 replicates for each time point. Hierarchical clustering was performed with euclidean distance and Ward’s minimum variance linkage algorithm. Metabolites were categorized according to Metabolon superpathways: Amino Acids, Carbohydrates, Cofactors & Vitamins, Energy, Lipids, Nucleotides, Peptides and Xenobiotics. To identify metabolites that show significant change over time and/or diet we used a linear regression model of the formula  $y \sim \beta_0 + \beta_1 * time + \beta_2 * diet + \beta_3 * diet * time + \epsilon$ . Significance of each fixed effect term in the linear model was estimated using ANOVA. Enriched KEGG pathways were identified using hypergeometric distribution test. Subpathway enrichments were calculated using Fisher’s exact test. To identify 24-hr cycling metabolites (Table S5), we used the nonparametric test JTK\_CYCLE (Hughes et al., 2010) using an adjusted p < 0.05 as described in (Abbondante et al., 2016; Eckel-Mahan et al., 2012). Subpathway enrichment analyses were performed applying Fisher’s exact test. For data entered into CircadiOmics, the rhythmicity test, BIO\_CYCLE is also used to define circadian oscillations, as described in (Agostinelli et al., 2016).

### Robust Correlations

To identify significant temporal correlations among metabolites in each tissue, we applied a robust permutation test, performing 100 random permutations of the replicate samples and estimated correlation coefficient and significance (Pearson correlation). Metabolites with a correlation pvalue < 0.05 in 95% (99% within tissue circos plots) of all permutation tests were considered as significant. Cross-tissue correlation networks were generated by connecting metabolites that show significant positive and negative correlations between tissues (Bonferroni corrected). Calculations were done using MATLAB and Statistics Toolbox R2016b.

### In vitro functional characterization of proton leak kinetics

HEK293 cells with stable expression of mouse UCP1 were generated as described (Jastroch et al., 2012). Briefly, mouse UCP1 ORF (NM009463) was cloned into pcDNA3.1. Subconfluent HEK293 cells were then transfected with either empty vector or mouse UCP1, and selected for stable transfection. Positive transfection was verified by western blot using rabbit anti-UCP1 polyclonal antibody (Chemicon #3046). Several aliquots of a clonal cell line were stored in liquid nitrogen to control for passaging effects. For proton leak measurements, an aliquot of UCP1 expressing and wild-type cells was seeded on a 10 cm cell culture dish. Cells were transferred to four 10 cm dishes after 3 days, and on day 5 seeded on 2 500 cm<sup>2</sup> dishes. Cell medium was replaced on day 7, and mitochondria were isolated on day 9. Proton leak kinetics were measured according to (Jastroch, 2012) by measuring mitochondrial membrane potential with a TPMP+ sensitive electrode simultaneously with oxygen consumption. In brief,

0.35 mg/ml of mitochondrial protein were incubated in buffer containing 0.3% defatted bovine serum albumin with either 500 uM inositol-monophosphate (IMP), or guanosine-monophosphate (GMP), or guanosine-diphosphate (GDP) for seven minutes before energization.

#### BAT qPCR

BAT mRNA was prepared from whole BAT tissue using Trizol (Invitrogen, 15596018). 1μg of RNA was used to synthesize cDNA using the Maxima H Minus cDNA Synthesis Master Mix (Thermo Scientific, M1662) and with an extension time of 60 min. at 50°C. qPCR was performed using SsoAdvanced Universal SYBR Green Supermix (Bio-Rad, 1725270) using the following parameters:

- 1) 95°C- 10 min.
- 2) 95°C- 30 s.
- 3) 60°C- 1 min.
- 4) 40 cycles of steps 2 and 3
- 5) 95°C- 15 s.

Amplification was performed using a QuantStudio 3 Real-Time PCR System. Analysis was performed using the  $2^{\Delta\Delta CT}$  method and data were normalized relative to 18SrRNA expression. Primer sequences can be found in [Table S6](#).

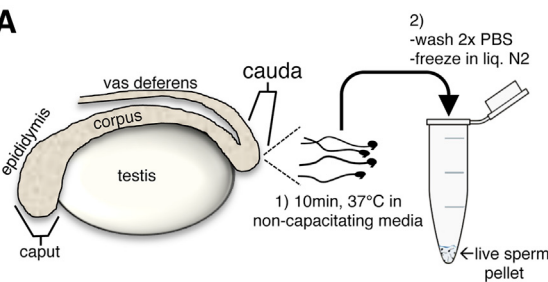
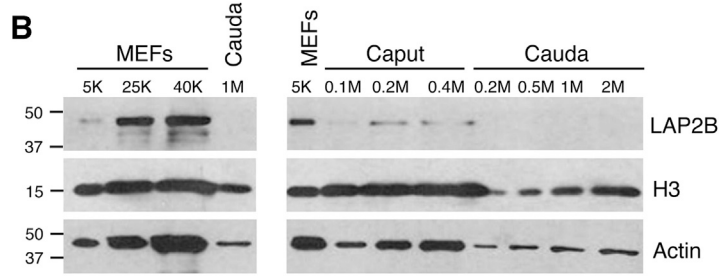
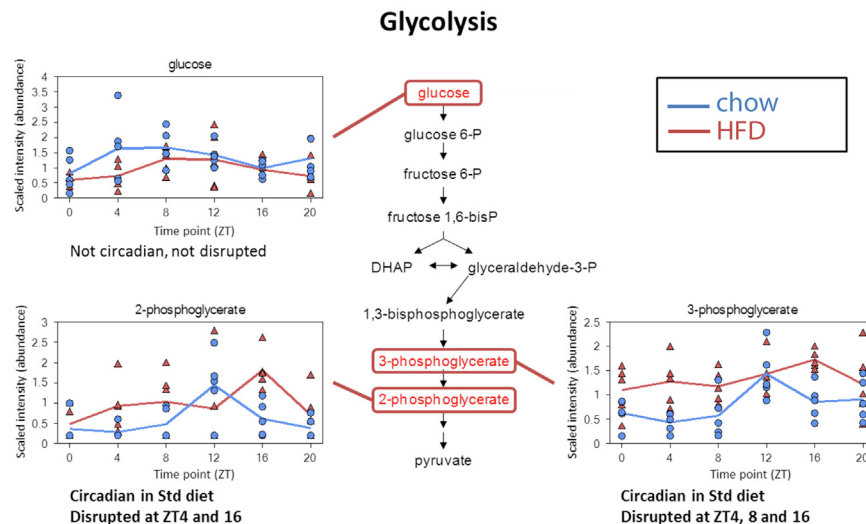
#### QUANTIFICATION AND STATISTICAL ANALYSIS

All data are expressed as means ± SEM unless stated otherwise. Statistical analysis was performed using a linear regression model or 2-way ANOVA. When ANOVA revealed significant genotype differences, further analysis was performed using Bonferroni's multiple comparison test. Differences between groups were considered statistically significant for p < 0.05.

#### DATA AVAILABILITY

All raw 24-h metabolomics intensity data ("origscale") has been deposited at (<https://doi.org/10.17632/zndtmk8xc6.1>), and can also be found in [Table S4](#). Elaborated metabolomics data are available from CircadiOmics (<http://circadiomics.igb.uci.edu>).

# Supplemental Figures

**A****B****C****D**

Lysolipid	ZT0	ZT4	ZT8	ZT12	ZT16	ZT20
1-palmitoylglycerophosphoethanolamine	1.54	0.99	1.32	0.91	1.03	1.32
2-palmitoylglycerophosphoethanolamine	1	1.02	1.06	0.56	0.9	0.41
1-stearoylglycerophosphoethanolamine	0.86	1.09	1.04	0.64	0.93	0.62
1-oleoylglycerophosphoethanolamine	1.14	1.03	1.21	0.74	0.97	1
2-oleoylglycerophosphoethanolamine	0.63	1.01	1.2	0.45	0.71	0.58
1-arachidonoylglycerophosphoethanolamine	1.13	0.85	1.01	0.91	1	1.18
2-arachidonoylglycerophosphoethanolamine	1.21	0.94	1.21	0.91	1.14	0.92
2-docosapentaenoylglycerophosphoethanolamine	0.7	1.3	1.01	0.57	0.96	0.56
2-docosahexaenoylglycerophosphoethanolamine	0.68	1.12	0.94	0.59	1.02	0.61
1-myristoylglycerophosphocholine	0.7	0.87	1.31	0.6	0.71	0.47
1-palmitoylglycerophosphocholine	0.78	1.13	1.22	0.54	0.87	0.53
2-palmitoylglycerophosphocholine	0.61	1.51	1.33	0.65	0.91	0.53
1-palmitoleoylglycerophosphocholine	0.66	0.86	0.62	0.64	0.84	0.74
1-stearoylglycerophosphocholine	0.81	1.11	1.06	0.58	0.89	0.6
2-stearoylglycerophosphocholine	0.71	1.2	1.01	0.88	0.91	0.52
1-oleoylglycerophosphocholine	0.64	1.12	1.17	0.57	0.85	0.57
2-oleoylglycerophosphocholine	0.59	1.23	1.1	0.52	0.81	0.63
1-linoleoylglycerophosphocholine	0.7	0.88	1.06	0.68	0.96	0.65
2-arachidonoylglycerophosphocholine	0.54	1.09	1.15	0.55	1.02	0.62
1-docosapentaenoylglycerophosphocholine	0.66	1.2	0.6	1.01	0.9	0.81
2-docosapentaenoylglycerophosphocholine	0.6	1.28	1.03	0.6	0.92	0.59
2-docosahexaenoylglycerophosphocholine	0.63	1.19	0.99	0.63	0.99	0.54
1-stearoylglycerophosphoinositol	1.27	1.07	1.59	0.88	1.04	0.88
1-palmitoylplasmenylethanolamine	1.3	1.13	1.14	0.77	0.94	1

(legend on next page)

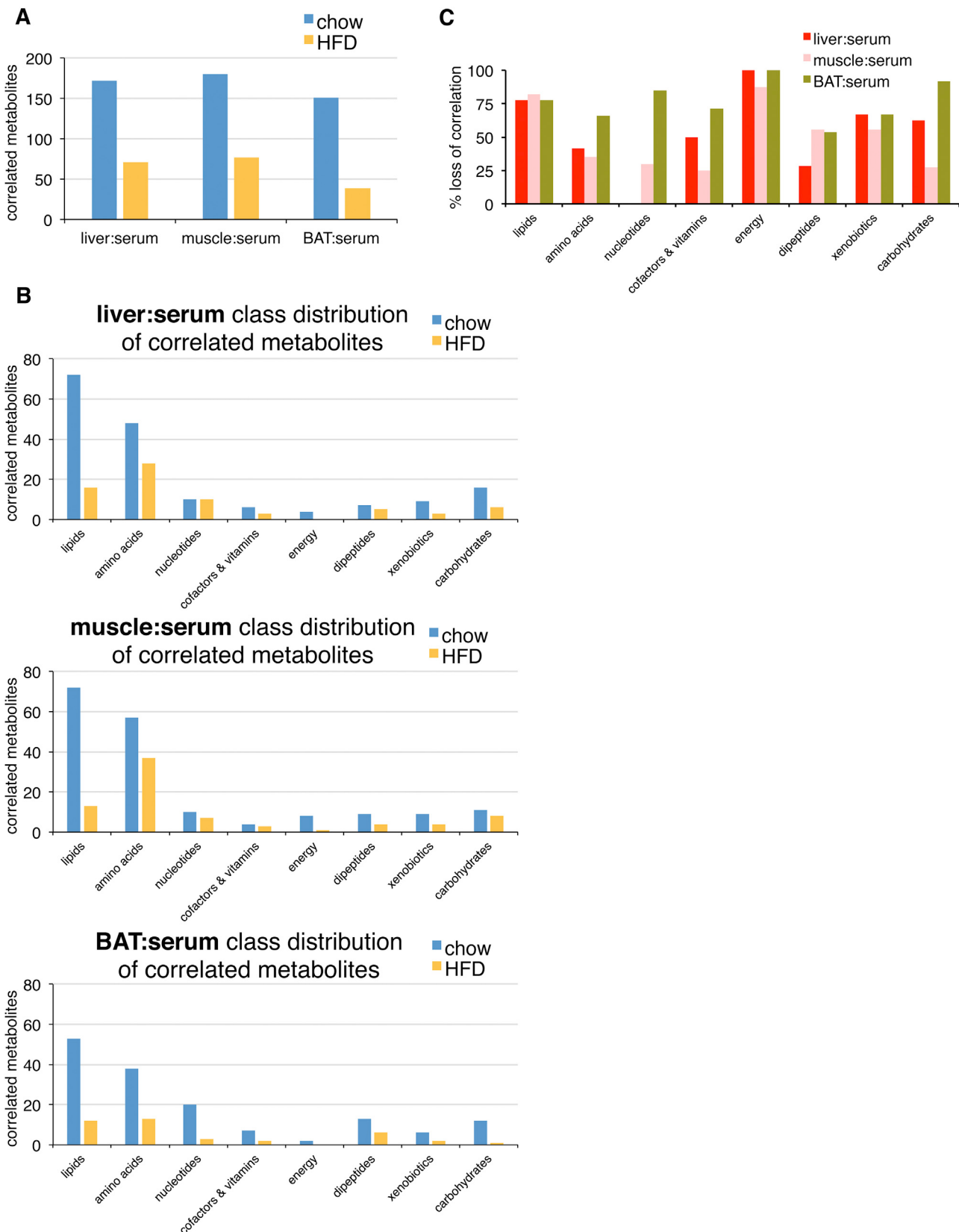
---

**Figure S1. Spermatozoa Collection and Summary, Related to Figure 1**

(A) Steps of spermatozoa collection.

(B) MEFs, Mouse Embryonic Fibroblasts, 5, 25 and 40 thousand cells; Caput, spermatozoa harvested from caput epididymis, 0.1, 0.2 and 0.4 million cells; Cauda, spermatozoa harvested from cauda epididymis, 0.2, 0.5, 1 and 2 million cells. LAP2B, lamina-associated polypeptide 2 $\beta$ , present in somatic cells and immature germ cells; H3, Histone H3 and Actin were used as loading controls.

(C and D) Main metabolite classes showing circadian function in mouse spermatozoa. (C) Graphs showing diurnal profiles of detected glycolytic intermediates. (D) Heatmap of detected lysolipids showing ratio of HFD/chow for each time point. Green cells indicate metabolites reduced by HFD (dark green,  $p \leq 0.05$ ; light green,  $0.05 \leq p \leq 0.1$ ; ANOVA). Pink cells indicate increased metabolites approaching significance ( $0.05 \leq p \leq 0.1$ ).

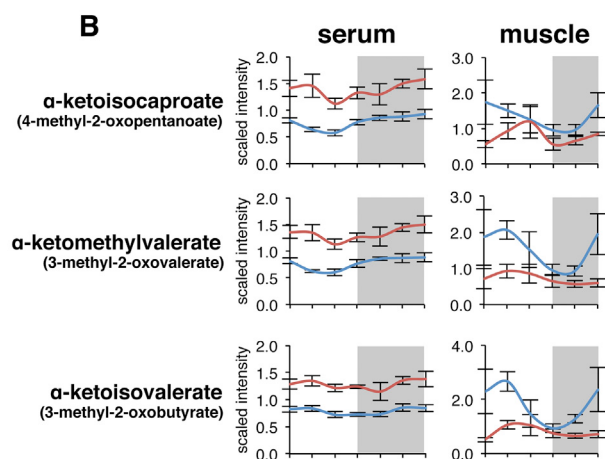
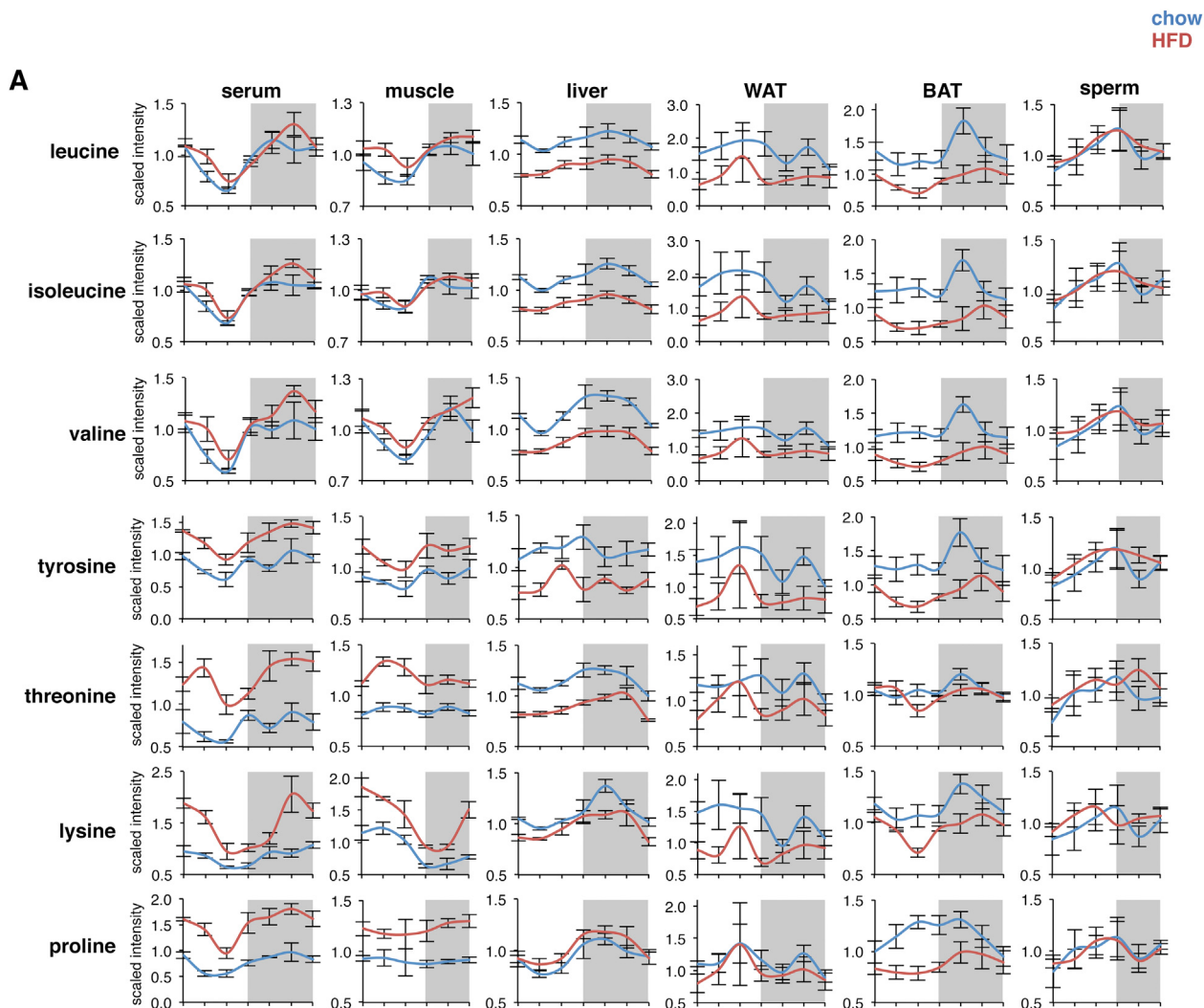


(legend on next page)

---

**Figure S2. Significant Cross-Tissue Correlations between Serum and Liver, Muscle, or BAT, Related to Figure 5**

- (A) Total number of correlated metabolites.
- (B) Metabolite class distribution of correlated metabolites between serum and liver, muscle or BAT.
- (C) Metabolite class distribution of lost correlations between serum and liver, muscle and BAT.



(legend on next page)

---

**Figure S3. Significant Cross-Tissue Correlations between Serum and Liver, Muscle, or BAT, Related to Figure 6**

(A and B) Diurnal variations of selected (A) amino acids and (B) branched-chain keto acids in mouse tissues under chow or HFD (mean  $\pm$  SEM; n = 5 per group per time point).

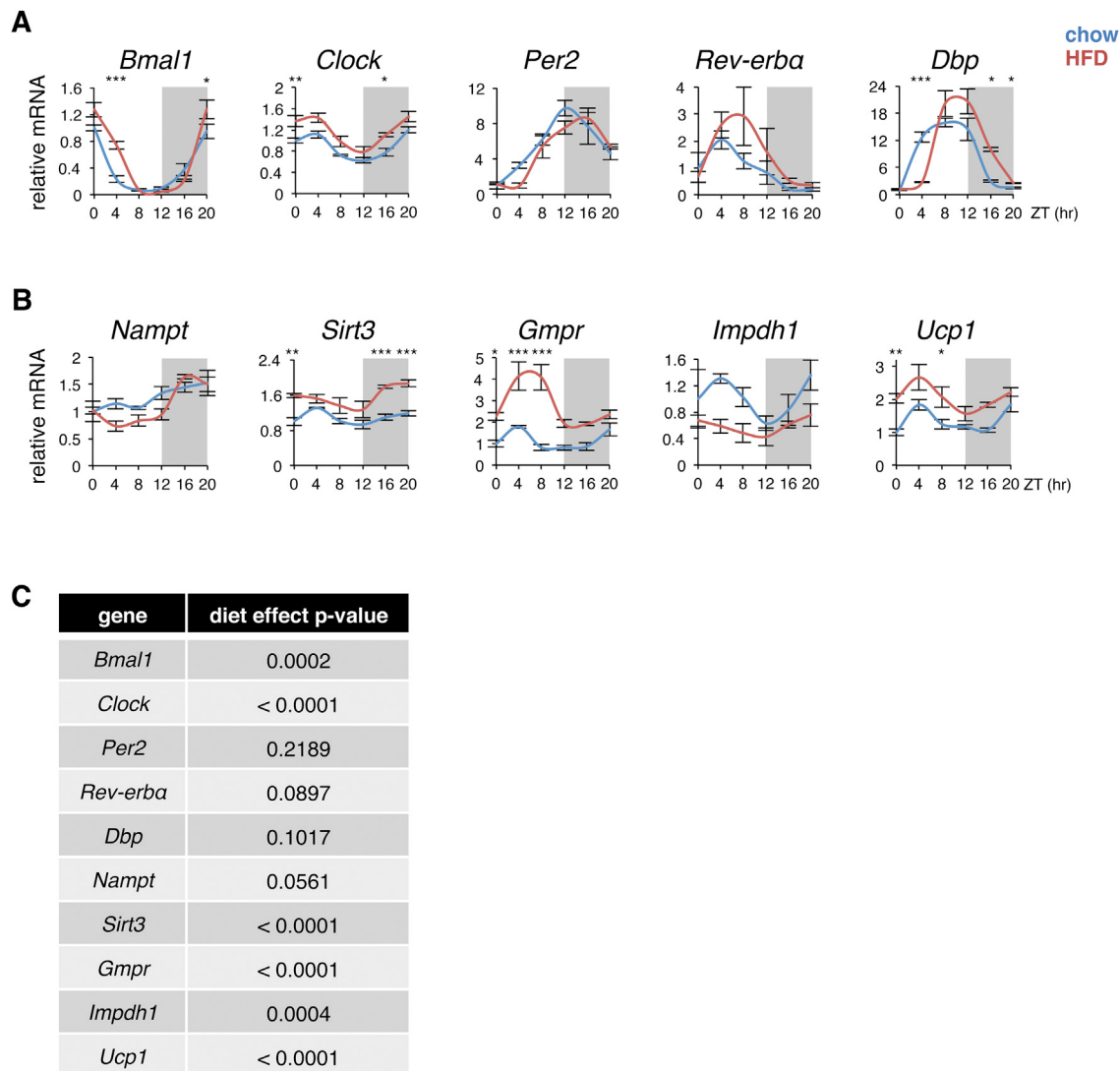


**Figure S4. High Fat Diet Alters 24-hr mRNA Expression Profiles of Circadian Genes in Brown Adipose Tissue, Related to Figure 7**

(A and B) Diurnal expression profiles of A) selected core circadian clock and B) selected circadian genes from brown adipose tissue (mean  $\pm$  SEM, expressed relative to 18S and normalized to chow ZT0; n = 4 per group per time point; \*p < 0.05, \*\*p < 0.01, \*\*\*p < 0.001, 2-way ANOVA with Bonferroni correction).  
(C) Diet effect p-values determined by 2-way ANOVA.